Burst-suppression in next-generation neural mass models and EEG

S.G.J. Lip
12-7-2023

Graduation Committee:
Dr. H.G.E. Meijer
Dr. S.M. Glas
Prof. Dr. Ir. M.J.A.M. van Putten
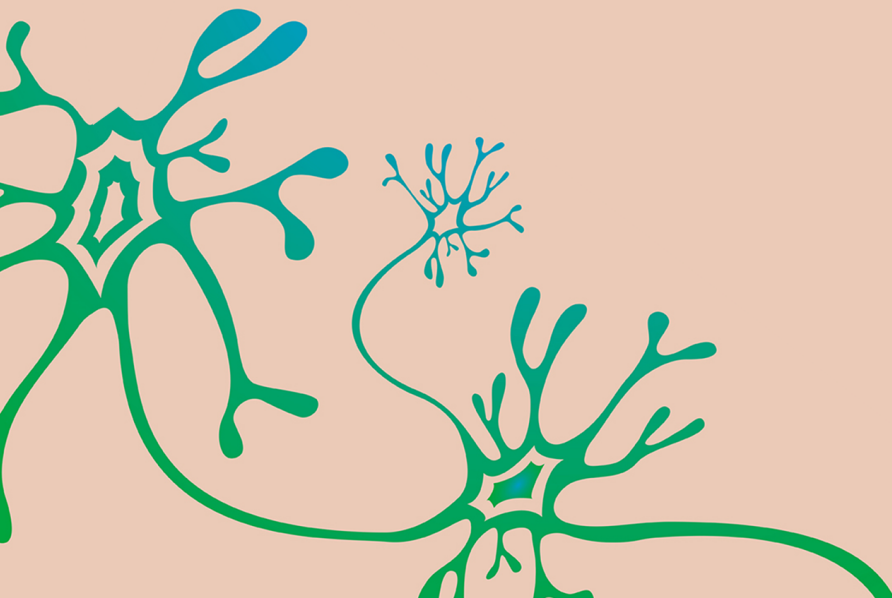
UNIVERSITY OF TWENTE.

Abstract

Introduction. The motivation for this project is a clinical phenomenon named burst-suppression (BS), which is a typical electroencephalogram (EEG) pattern seen in patients during postanoxic coma. It is characterised by an alternation of bursts of activity and iso-electricity. Two types exist, BS with identical bursts (BSIB) and BS with non-identical bursts (BSNIB). The mechanisms underlying BS and the differences between BSIB and BSNIB are poorly understood. Neuronal network models are adequate tools for investigating mechanisms underlying observed behaviour of neuronal populations. The recently developed next-generation neural mass models directly relate microscopic network properties to macroscopic observables that approximate EEG. Here, we investigate the role of sparse synaptic coupling in the emergence of BSNIB.

Methods. We implement a spiking neural network of 10^4 Quadratic-Integrate-and-Fire (QIF) neurons, and derive its exact low-dimensional mean-field representation, the next-generation neural mass model. We describe realistic chemical and electrical synaptic connections between neurons, and spike-frequency adaptation (SFA). In addition, we extend our single excitatory population with a population of inhibitory QIF-neurons. In these models, we identify bursting dynamics, and analyse the similarity of bursts within simulations where we decrease the synaptic coupling probability (p_{Syn}) stepwise. Finally, we visually compare model simulations with EEG.

Results. In the one- and two-population model, a fold-fold burster exists. A realistic number of gap junctions per neuron had a negligible effect on the burst pattern. Simulations of networks with all-to-all synaptic coupling showed small burst similarity values, caused by large differences in the neuron-specific adaptation variables. Reducing the synaptic coupling probability p_{Syn} caused an increase in burst similarity within a simulation. In the model with two populations, the intrinsic activity level of the inhibitory population distinguishes two types of bursting dynamics. High inhibitory activity induces rest state oscillations and lower burst similarity values for all p_{Syn}. Some simulations show a tentative resemblance with BSIB EEG, but none resemble BSNIB.

Discussion. The approximation of individual SFA by population SFA is invalid. The failure of this assumption causes the microscopic model behaviour to deviate from the neural mass equivalent, also in the two-population model. Still, the two-population model shows remarkable bursting dynamics, where the rest state oscillations could play an important role in finding model behaviour with non-identical bursts. Future research should focus on a different slow modulatory mechanism to facilitate bursting, and on a more thorough exploration of the dynamics of the two-population model. Tuning inhibition and adding population noise are important steps towards finding BSNIB in a neuronal network model.

Contents

1 Introduction

This project is a computational study of bursting behaviour in spiking neuronal networks with sparse coupling. It is motivated by a clinical phenomenon that is observed on the electroencephalogram (EEG) of comatose patients, called burst-suppression (BS). We introduce this clinical phenomenon, discuss how researchers use modern computational models of the brain to investigate neurological phenomena such as BS, and formulate the objective that underlies our project.

1.1 Burst-suppression

Burst-suppression is a typical EEG pattern that emerges in a variety of physiological and pathological conditions [1, 2]. This EEG pattern is characterised by its spatially synchronous progression, where the signal is an alternation of short, high amplitude bursts and longer periods of low amplitude activity or even isoelectricity [3]. Two types of BS can be distinguished: BS with identical bursts (BSIB), which is uniquely seen in patients in postanoxic coma [3], and BS with non-identical bursts (BSNIB), which is observed in several different conditions, including postanoxic coma, anesthesia, and therapeutic hypothermia [1, 2]. BSIB is a highly specific predictor for poor neurological outcome after postanoxic coma [3].

In Figure 1, we show short epochs of EEG with burst-suppression from patients in a postanoxic coma. Figure 1a shows the onset of two successive bursts that are non-identical. It is difficult to identify the exact moment of burst onset, since multiple channels show a gradual burst initiation. Also, the increase in activity is only partially synchronous across all channels. Figure 1b shows two successive identical bursts. Between the two bursts, the timing and amplitude of peaks are highly similar. Here, as opposed to the non-identical bursts, there is a clear moment of burst onset, with an initial fast rise in amplitude. The bursts emerge with a high level of spatial synchrony.

The mechanisms underlying the distinctive BS pattern on the EEG are still poorly understood. However, several hypotheses exist regarding the neurophysiology that induces BS. The metabolic hypothesis, which proposes that BS originates from a neurometabolic deficit, has been extensively documented [2, 4]. In short, energy deprivation would underlie BS through decreased activity

(a) Non-identical bursts   **(b)** Identical bursts
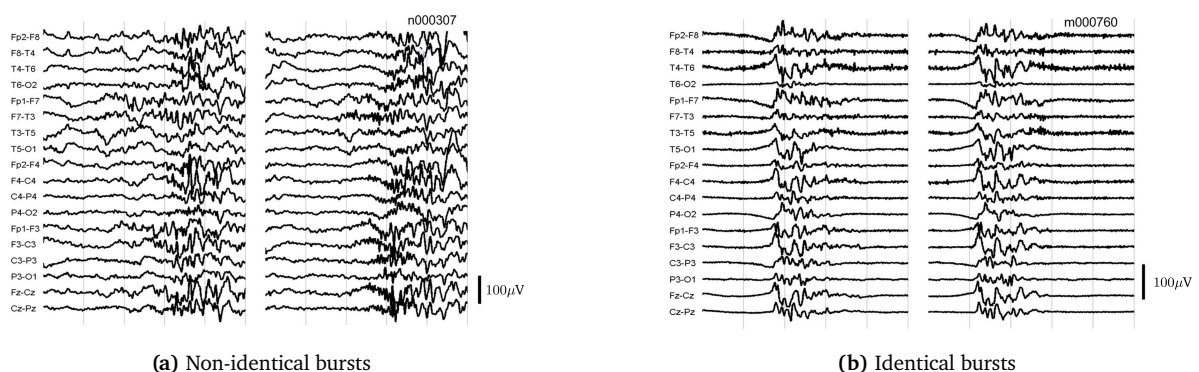
Figure 1: Two examples of burst-suppression on the EEG, adapted from [3]. In (a), the onsets of two non-identical bursts from a pattern of BSNIB are shown. In multiple channels, small oscillations occur before the burst starts. The burst onset is not entirely synchronous across all channels, in both bursts. This opposes the identical bursts in (b), which have a clear spatially synchronous onset. These bursts start abruptly and simultaneously across all channels. Within a channel, the two bursts are extremely similar. All four epochs have a 5 second duration. The EEGs in (a) and (b) where recorded from different patients.

3

of ATP-dependent cellular transporters. Inhibition is expected to play a significant role in the emergence of BS, since it is prominent in both postanoxic and anesthesia-induced coma, through the selective suppression of excitatory synapses [5] and increased inhibitory activity, respectively. An alternative hypothesis is built upon evidence of a hyperexcitable brain during anesthesia-induced BS [6–8], where decreased inhibitory activity is argued to be the origin of BS. Opposing a unifying responsible mechanism for the emergence of BS, some suggest that the mechanisms causing BS differs per pathological condition [3].

1.2 Models of neuronal networks

The use of mathematical models to gain knowledge of physiological mechanisms that cause clinical observations such as BS is strongly endorsed. In general, brain dynamics can be modelled on two scales: a microscopic scale, where we define a model of individual neurons and connect these by synapses to construct a network, and a global scale, where we define mean-field models of populations of neurons that describe the mean activity of such populations. Relating these models to *in vitro* or *in vivo* experimental observations may provide valuable insight into the functioning of the brain in physiological and pathological conditions.

1.2.1 Microscopic models

Modelling neurons on a microscopic scale starts by describing the electrical properties of the neuronal cell membrane. The central state variable of a modelled neuron is its membrane potential, whose evolution is driven by transmembrane currents. Our intricate knowledge of molecular neurophysiology allows describing detailed models of individual neurons, building on the work of Hodgkin and Huxley [9]. These models, characterised by an accurate description of the ion dynamics involved in neuronal signalling, are useful for investigating the effects of microscopic changes in neuronal physiology.

For modelling network phenomena such as BS, we often use simpler phenomenological models that describe the spiking behaviour of neurons. These spiking neuron models describe the neuronal action potential, but do not describe the ion dynamics that underly their formation. Models of spiking neurons can be connected by (modelled) synapses to form spiking neural networks. We use these networks to investigate the behaviour of populations of neurons. An example of a spiking neuron, the building block for a spiking neural network, is the Quadratic-Integrate-and-Fire (QIF) neuron. This neuron model is, in its simplest form, described by the following ordinary differential equation:

$$\dot{V}(t) = (V(t))^2 + I(t), \tag{1.1}$$

with the following reset rule: if $V > V_{\text{thr}}$, a spike is emitted and $V \leftarrow V_{\text{reset}}$, where $V_{\text{thr}}, V_{\text{reset}} \in \mathbb{R} \cup \{\pm\infty\}$. The QIF-neuron is defined by its membrane potential $V(t)$, and it is driven by the square of $V(t)$ and a term $I(t)$ that describes the sum of incoming currents.

The behaviour of a single QIF-neuron is easy to analyse, and underpins the behaviour of a network of QIF-neurons. The single QIF-neuron behaviour is determined by its fixed point structure, which depends on $I(t)$. This fixed point structure thus possibly varies in time. For the following, we remove this time dependence, i.e. we assume $I(t) = I$, and in addition, we assume $V_{\text{thr}} > |I|$ and $V_{\text{reset}} < -|I|$. The value of I now determines the number of fixed points. If $I < 0$, two equilibria exist, a stable one at $V = -\sqrt{-I}$ and an unstable one at $V = \sqrt{-I}$. When the initial condition $V_0 > \sqrt{-I}$, the neuron spikes once, is reset to $V = V_{\text{reset}}$, and then converges to the stable equilibrium at $V = -\sqrt{-I}$. When $V_0 < \sqrt{-I}$, the neuron converges to $V = -\sqrt{-I}$ without spiking. When I is increased, at $I = 0$ the two equilibria merge to a neutral fixed point, with still the same behaviour as for $I < 0$. For $I > 0$, no equilibria exist and the neuron is in a regime of sustained spiking. The behaviour of V for different values of I is shown in Figure 2.

In the spiking regime, the firing rate is a function of I. We obtain this firing rate equation by integrating (1.1) over one cycle, from $V(t_0) = V_{\text{reset}}$ to $V(t_0 + T) = V_{\text{thr}}$, where T is the period
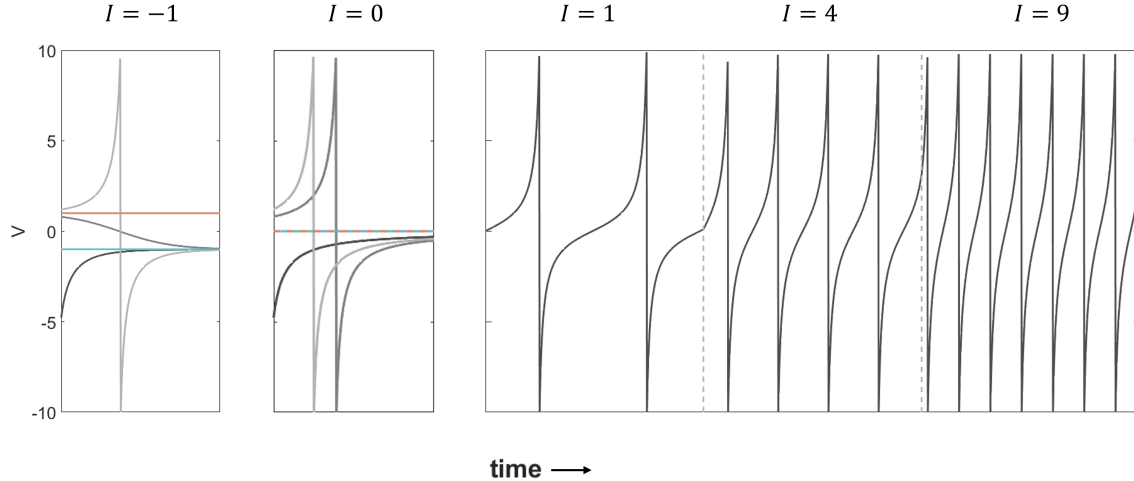
Figure 2: Behaviour of V for a single QIF-neuron, for different values of input current I. With $I = -1$, there are two equilibria, a stable one in blue at $V = -1$ and an unstable one in red at $V = 1$. Solutions with initial conditions $V_0 < 1$ directly converge to the stable equilibrium without spiking, when $V_0 > 1$ one spike is emitted before convergence to the stable equilibrium. At $I = 0$ the two equilibria merge, making it attracting from below, but repelling from above. Solutions with the same initial conditions as for $I = -1$ are shown. All solutions eventually settle at $V = 0$, only after emitting one spike if $V_0 > 0$. A last simulation where I was increased stepwise, from $I = 1$ to $I = 4$ to $I = 4$ shows the dependence of the firing rate on I. Compared to $I = 1$, the firing rate doubled after the increase to $I = 4$, and tripled after the increase to $I = 9$. All simulations were performed with finite $V_{\text{thr}} = -V_{\text{reset}} = 10$.

of firing, and the firing rate is $f = 1/T$. For arbitrary V_{thr} and V_{reset}, the firing rate equation is given by

$$f(I) = \sqrt{I} \left(\arctan \frac{V_{\text{thr}}}{\sqrt{I}} - \arctan \frac{V_{\text{reset}}}{\sqrt{I}} \right)^{-1}. \tag{1.2}$$

Choosing $V_{\text{thr}} = -V_{\text{reset}} \to \infty$ reduces this equation to $f(I) = \frac{1}{\pi}\sqrt{I}$. This firing rate curve and one for $V_{\text{thr}} = -V_{\text{reset}} = 10$ are shown in Figure 3.

One important component of I is the synaptic current. Synapses can be divided into two classes: chemical synapses and electrical synapses. A chemical synapse is a unidirectional connection, most often axodendritic, that processes a presynaptic spike to a postsynaptic current. Connections might be bidirectional, but via two separate synapses. The easiest way to model a chemical synapse is by describing it as a product of a synaptic coupling strength and a synaptic activation variable. The electrical synapse, also called gap junction, is a bidirectional connection between two neurons that couples their membrane potential. It is modelled as the product of a coupling strength and the difference between the membrane potentials of both neurons.

1.2.2 Mean-field models and next generation neural masses

Mean-field models of the brain find their origin in the work of Wilson and Cowan [10]. This type of model describes the mean membrane potential of a population of neurons, also called a neural mass. The mean membrane potential of a population of cortical pyramidal cells approximates the current dipole that is generated by these cells, which is, passing intermediate steps, captured by EEG measurements. The low dimension of these models makes them highly suitable for mathematical analysis, providing insight into the population parameters that induce changes in the macroscopic observables. Single neural masses are extended to coupled neural masses describing e.g. thalamocortical circuits, to neural field models incorporating the spatial propagation of brain activity, to extensive whole brain network models [11–15].

In these classical neural mass models, the mean membrane potential defines the state of the population, and the firing rate is assumed to be a sigmoidal function of the mean membrane
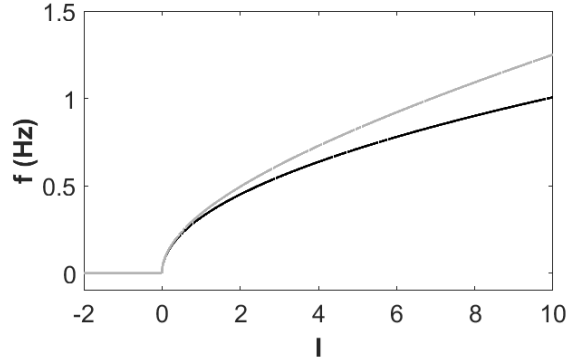
Figure 3: The firing rate of a QIF-neuron as a function of the current I. In black, we show $f(I)$ for $V_{\text{thr}} = -V_{\text{reset}} = \infty$, with the formula $f(I) = \frac{1}{\pi}\sqrt{I}$ for $I > 0$. In grey, we show $f(I)$ for $V_{\text{thr}} = -V_{\text{reset}} = 10$, given by Eq. (1.2). The grey curve gives the firing rates of the simulations in Figure 2.

potential. Since this relation between firing rate and mean membrane potential is based on experimental observations, the classical neural mass models have a phenomenological nature. Recently, a new type of neural mass model was proposed, where the firing rate of a population is derived exactly from the microscopic properties of the underlying network. This next-generation neural mass model was first described by Montbrio et al. [16], building on the work of Ott and Antonsen [17] on a low dimensional representation of an ensemble of θ oscillators. The insight in [16] was that a θ oscillator can be transformed to a QIF-neuron, from which they showed that the Ott-Antonsen (OA) ansatz for dimensionality reduction also applies to a network of QIF-neurons connected by instantaneous synapses. For the resulting system of firing-rate equations, they analytically identified parameter regions of bistability. They concluded with a description of interacting excitatory and inhibitory populations, without further analysing the behaviour of this extended system.

Toward a more realistic microscopic network description, Byrne et al. [18] incorporated the α-synapse for connections between QIF-neurons, and showed that this preserves the applicability of the OA ansatz. In addition to chemical synapses, also electrical synapses, or gap junctions, have been incorporated in next-generation neural mass models [19–21]. Gap junctions are shown to induce oscillatory behaviour for suitable parameter settings, suggesting that this type of synapse enhances synchrony between neurons. Synchrony has also been studied in next-generation neural mass models on a population level, with two symmetric populations [22], one excitatory and one inhibitory population [21], up to three different populations [23]. Furthermore, neuronal fatigue mechanisms were introduced into next-generation neural mass models. Common choices for these mechanisms are short-term synaptic depression (STP) [23–25] and spike-frequency adaptation (SFA) [22, 26]. This fatigue acts on a much slower timescale than membrane potential dynamics. Addition of such slow modulatory mechanisms potentially induces bursting [26, 27].

1.3   Models of bursting and burst-suppression

BS is a clinical example of bursting. The work of Izhikevich gives a vast theoretical description of bursting in excitable systems [28]. A neuronal burster consists of a fast subsystem that is responsible for the spiking behaviour, and a slow variable that induces switches from a rest state to an active state, and back. Two key bifurcations in the fast subsystem define the type of burster: the bifurcation of the rest state, where the solution goes from the rest state to the active state, and the bifurcation of the active state, where the solution returns to the rest state. This bifurcation of the active state is often a bifurcation of a limit cycle, e.g. a homoclinic, fold of limit cycles, or Hopf bifurcation. However, Izhikevich also describes a fold-fold burster, where the bifurcation of the rest state and the active state are both normal fold bifurcations. Here, the active state is a

fixed point with a weak rate of convergence, causing damped oscillations in the neighbourhood of the fixed point. The bifurcation structure of the fast subsystem gives insight into the bursting behaviour of the full system. Therefore, slow-fast analysis by separating the slow and fast dynamics of a system is a widely applied technique for analysing bursters [25, 29].

Bursting in terms of BS has been studied in multiple computational studies, with different approaches [29–31]. The earliest [30] describes a phenomenological nonlinear model with simulations considerably similar to BS EEG. However, they do not discuss physiological mechanisms that might underlie BS because of the absence of biophysical parameters in their model. In [31], a network of fourteen Hodgkin-Huxley type cells, both excitatory and inhibitory, was modelled. To test the metabolic hypothesis for BS, the model included ATP dynamics. The results showed that a reduction in cerebral metabolic rate and thus a reduced availability of ATP, e.g. due to oxygen deprivation during an ischemic event, gave rise to BS-like patterns. By the scale of this network, the results are not directly comparable to EEG. To bridge this gap, Liley et al. [29] developed a cortical mean-field model, of which the mean-field membrane potential is considered an approximation of EEG. This enables a direct comparison of simulations to clinical observations. The slow modulatory process in the Liley model is short-term synaptic depression. Although this model describes neuronal populations and can thus be related to neuroanatomical features, it lacks a relation to microscopic physiological parameters such as synaptic connections between individual neurons. As described above, next-generation neural mass models incorporate these aspects in the mean-field description.

1.4 Project objective

The next-generation neural mass model is a strong analytical and experimental tool, but the necessary assumptions for this reduction are not all physiologically plausible. Especially the assumptions of all-to-all coupling and unimodal synchronization of neurons are unrealistic in neuronal populations *in vivo*. To be able to relate model simulations to clinical data, we must investigate the effect of realistic, sparse coupling between neurons on model behaviour. Moreover, we hypothesise that these properties of the neuronal network play an important role in the emergence of BSNIB. Breakdown of the exact correspondence of the microscopic model to the mean-field model is crucial for finding BSNIB, since the non-identical bursts clearly do not follow a single population mean. This is substantiated by previous studies, where simulations of microscopic networks show that finite-size effects and variation in connectivity give rise to patterns that are comparable to BSNIB [32–35]. The role of suppression or failure of synaptic communication in BS motivates investigating the effect of variations in synaptic coupling. We hypothesise that clustered activity underlies the variations in burst shape seen in BSNIB. Building towards a more physiologically realistic model, we incorporate α-synapses, SFA, and gap junctions in our neuronal network and study their effect. In addition, we extend the excitatory one-population model with a second inhibitory population. We start by analysing our mean-field model and continue with simulations of the microscopic model for different network architectures.

We will answer the following research question: what are the effects of variations in network architecture and implemented model components on the behaviour of the microscopic model, and when do variations lead to behaviour of the microscopic model that diverges from the mean-field equivalent? In other words, when do solutions of the microscopic model no longer follow a uniform population mean? In the end, we aim to translate the identified variations to a clinically relevant conclusion: what conditions can be identified for the emergence of burst-suppression with non-identical bursts in a network of Quadratic-Integrate-and-Fire neurons?

2 Methods

The core of our project is a detailed microscopic spiking neuronal network model and its next-generation neural mass equivalent. We describe these two models, and show how the microscopic model reduces to the neural mass model. In numerical experiments, we will compare the bursting behaviour of the neural mass model to that of the microscopic model with different settings for synaptic coupling. We designed a burst detection algorithm, and implemented a known method to measure the similarity between individual bursts [3].

2.1 Neuronal network models

Our microscopic model and neural mass model are based on [16], incorporating a combination of additional mechanisms from [18, 26]. The description of the microscopic model includes the network architecture, to which we introduce sparse synaptic coupling.

2.1.1 Spiking neural network

As our microscopic model, we consider a network of N Quadratic Integrate-and-Fire (QIF) neurons, characterised by their membrane potentials $\{V_j\}_{j=1,\dots,N}$ that evolve according to a first-order Ordinary Differential Equation (ODE) with reset:

$$\tau \dot{V}_j(t) = (V_j(t))^2 + \eta_j + Js_j(t)\tau + \kappa g_j(t) + I(t),$$
$$\text{if } V_j(t) > V_{\text{thr}}, \ V_j(t) \leftarrow V_{\text{reset}}, \tag{2.1}$$

where V_{thr} denotes the spiking threshold, i.e. when $V_j(t)$ reaches V_{thr} neuron j emits a spike, and V_{reset} denotes the reset potential after a spike. In our analysis, we consider the limit $V_{\text{thr}} = -V_{\text{reset}} \to \infty$. The input current consists of four components: a heterogeneous, constant input current η_j drawn from a distribution $L(\eta)$ that we define later, a synaptic input current given by the product $Js_j(t)$, a gap junction current $\kappa g_j(t)$, and a common, time-varying input current $I(t)$. The membrane time constant is denoted by τ.

The synaptic current is the product of the synaptic connection strength, J, and the mean of the synaptic activation of the incoming synapses, s_j. The latter is given by

$$s_j(t) = \frac{1}{|S_j|} \sum_{n \in S_j} \sum_{k, t_n^k < t} \int_{-\infty}^{t} a(t - t')\delta(t' - t_n^k) \, dt'.$$

The set S_j denotes all neurons that have an efferent connection to the dendritic tree of neuron j, $a(t)$ denotes the synaptic kernel function, and $\delta(t)$ denotes the Dirac delta function. The kth spike time of neuron n is denoted by t_n^k. The synaptic kernel function describes the response of a synapse to an incoming action potential, and it is characterised by a rise rate α_r, and a decay rate α_d. Often, we assume infinitely fast synapses, i.e. the rise and decay rates go to infinity, which corresponds to $a(t) = \delta(t)$. A more realistic assumption is $\alpha_r = \alpha_d = \alpha$, where the kernel function has the form $a(t) = \alpha^2 t e^{-\alpha t}\Theta(t)$, with $\Theta(t)$ the Heaviside step function to ensure causality. Both kernel functions are the Green's function of a linear differential operator that we denote by Q, by which we describe the evolution of $s_j(t)$ as an ODE:

$$Qs_j(t) = \frac{1}{|S_j|} \sum_{n \in S_j} \sum_{k, t_n^k < t} \delta(t - t_n^k). \tag{2.2}$$

The case $a(t) = \delta(t)$ yields $Q = 1$, whereas $a(t) = \alpha^2 t e^{-\alpha t}\Theta(t)$ yields $Q = (1 + \frac{1}{\alpha}\frac{d}{dt})^2$.

The gap junction current is the product of the connection strength κ, and the gap junction variable g_j, which is given by:

$$g_j(t) = \frac{1}{N} \sum_{m \in G_j} (V_m(t) - V_j(t)). \tag{2.3}$$

The set G_j denotes all neurons that have a gap junction connection to neuron j.

Macroscopic observables of this system are the mean membrane potential, defined by

$$\bar{v}(t) = \frac{1}{N} \sum_{j=1}^{N} V_j(t),$$

and the mean firing rate, defined by

$$\bar{r}(t) = \frac{1}{N} \sum_{j=1}^{N} \sum_{k \in \mathbb{Z}} \delta(t - t_j^k).$$

All separate N neurons form an interconnected network through chemical synapses and gap junctions between neurons. By defining these connections, we impose a structure on the network. For now, we assume all-to-all coupling, i.e. each neuron is connected to all other neurons through both chemical synapses and gap junctions. This includes self-connections. Note that, although self-connecting gap junctions do not exist, this does not impair our definition: by Eq. 2.3, the gap junction current between a neuron and itself always equals zero.

Under the assumption of all-to-all coupling, the evolution equations of $s_j(t)$ and $g_j(t)$ reduce to

$$Qs_j(t) = \bar{r}(t),$$

and

$$\kappa g_j(t) = \kappa \bar{v}(t) - \kappa V_j(t). \tag{2.4}$$

2.1.2 Mean-field model

Under several assumptions, the network described above allows a substantial dimensionality reduction. In the limit $N \to \infty$ and assuming all-to-all coupling of the neurons, we describe the membrane potentials of neurons with the same η by a continuous probability density function $\phi(V|\eta, t)$. Note that the time-dependency of V is now transferred to a time-dependency of its distribution given η. Conservation of the number of neurons yields the following continuity equation:

$$\partial_t \phi = -\partial_V \phi \dot{V}, \tag{2.5}$$

with $\dot{V}$ the V-dependent function defined in (2.1) after substitution of (2.4), and where we have dropped the index j. By ∂_t and ∂_V we denote the partial derivatives with respect to variables t and V, respectively. Without temporal forcing and without inter-neuronal connections, i.e. $I = 0$ and $J = \kappa = 0$, Eq. (2.5) has a trivial stationary solution $\phi_0(V|\eta) \propto (V^2 + \eta)^{-1}$. The form of this solution corresponds to that of a Lorentzian function, which provides an intuition for the ansatz that follows. This ansatz, known as the Ott-Antonsen ansatz [17], assumes that, in the limit $N \to \infty$, $\phi(V|\eta, t)$ converges to a Lorentzian-shaped function in general, i.e. also in the presence of time-varying currents. By this assumption, we define:

$$\phi(V|\eta, t) = \frac{1}{\pi} \frac{x(\eta, t)}{(V - y(\eta, t))^2 + x(\eta, t)^2}, \tag{2.6}$$

where $y(\eta, t)$ denotes the center of the distribution, and $x(\eta, t)$ the half-width-at-half-maximum (HWHM) of this distribution. This is the general form of a Lorentzian function. A possible graph
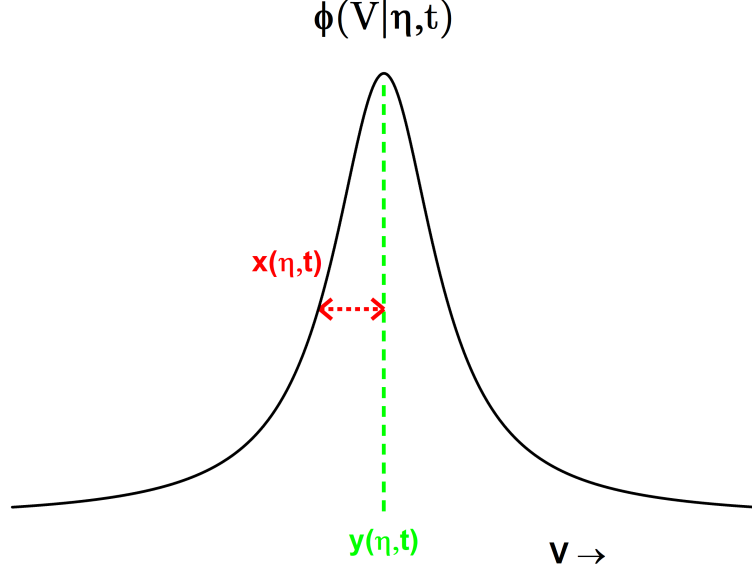
Figure 4: Graph of a Lorentzian distribution $\phi(V|\eta, t)$, defined by (2.6), where $y(\eta, t)$ denotes the center of the distribution, $x(\eta, t)$ denotes the half-width-at-half-maximum. The Lorentzian distribution is a unimodal distribution, whose single peak's location and height are determined by $y(\eta, t)$ and $x(\eta, t)$, respectively.

of $\phi(V|\eta, t)$ and its dependence on V, $x(\eta, t)$ and $y(\eta, t)$ is shown in Figure 4. We thus assume a unimodal distribution of the membrane potentials given a value of η. In terms of synchrony, a peaked distribution (i.e. $x(\eta, t)$ is small) translates to synchronous activity of neurons, whereas a flat distribution (i.e. $x(\eta, t)$ is large) corresponds to asynchrony.

The distribution parameters $y(\eta, t)$ and $x(\eta, t)$ are directly related to the macroscopic observables of the system: the mean membrane potential and mean firing rate. In terms of the distribution, the mean membrane potential equals the center of the distribution $y(\eta, t)$, since (2.6) is symmetric in $y(\eta, t)$. We interpret the mean firing rate as the rate at which neurons cross $V_{\text{thr}} \to \infty$, which yields:

$$r(\eta, t) = \left. \phi(V|\eta, t)\dot{V}(V|\eta, t)\right|_{V \to \infty},$$
$$= \frac{1}{\pi\tau}x(\eta, t).$$

To get rid of the η-dependence of $v(\eta, t)$ and $r(\eta, t)$, we must assume a distribution for η. In the limit $N \to \infty$, the η_i's are described by a continuous distribution that we denote by $L(\eta)$. Given this distribution, we integrate over all values of η to obtain expressions for $v(t)$ and $r(t)$ in terms of the membrane potential distribution parameters:

$$v(t) = \int_{-\infty}^{\infty} y(\eta, t)L(\eta)\,d\eta, \tag{2.7}$$

$$r(t) = \frac{1}{\pi\tau} \int_{-\infty}^{\infty} x(\eta, t)L(\eta)\,d\eta. \tag{2.8}$$

The next step is to substitute (2.6) into the continuity equation (2.5). Without explicitly indicating the η- and time-dependence of x and y, simplifying the left-hand-side yields:

$$\partial_t\phi = \frac{\partial_t x\left((V-y)^2 - x^2\right) + \partial_t y\left(2xV - 2xy\right)}{\pi\left((V-y)^2 + x^2\right)^2}.$$

10

Collecting the factors in the numerator above, the right-hand-side reduces to:

$$-\partial_V\phi\dot{V} = \frac{1}{\tau}\frac{2x(V-y)(V^2+\eta+Js\tau+\kappa v-\kappa V+I)-(2xV-\kappa x)\left((V-y)^2+x^2\right)}{\pi\left((V-y)^2+x^2\right)^2},$$

$$= \frac{1}{\tau}\frac{(2xy-\kappa x)((V-y)^2-x^2)+(\eta+Js\tau+\kappa v-\kappa y+I-x^2+y^2)(2xV-2xy)}{\pi\left((V-y)^2+x^2\right)^2}.$$

By identifying the common terms $(V-y)^2-x^2$ and $2xV-2xy$ in the equations for $\partial_t\phi$ and $-\partial_V\phi\dot{V}$, and equating the preceding terms, we find that the following expressions for $\partial_t x$ and $\partial_t y$ solve (2.5):

$$\tau\partial_t x = 2xy-\kappa x, \tag{2.9}$$

$$\tau\partial_t y = \eta+Js\tau+\kappa v-\kappa y+I-x^2+y^2. \tag{2.10}$$

Next, for the evaluation of the integrals in (2.7) and (2.8), we must make an assumption on $L(\eta)$, the distribution of η. The largest dimensionality reduction is obtained when we assume $L(\eta)$ is a Lorentzian distribution, that we define by:

$$L(\eta) = \frac{1}{\pi}\frac{\Delta}{(\eta-\eta_0)^2+\Delta^2}. \tag{2.11}$$

Here $\eta_0\in\mathbb{R}$ is the center of the distribution, and $\Delta\in\mathbb{R}_+$ is the HWHM of this distribution. Note that $L(\eta)$ has two poles, at $\eta_\pm=\eta_0\pm i\Delta$. We will exploit this useful property to solve the integrals by contour integration.

First, we need to define the complex variable $w(\eta,t):=x(\eta,t)+iy(\eta,t)$, whose time-derivative is found using (2.9) and (2.10):

$$\tau\partial_t w = -\kappa w+i(\eta+Js\tau+\kappa v-w^2+I). \tag{2.12}$$

We expand this $w(\eta,t)$ into complex valued $\eta=\eta_r+i\eta_i$, after which the real part of (2.12) reads $\tau\partial_t x = -\kappa x+2xy-\eta_i$. This guarantees that in the entire lower half complex plane, the width of the distribution satisfies $x(\eta,t)\geq 0$, because at $x=0$ we have $\partial_t x=-\frac{\eta_i}{\tau}>0$ for $\eta_i<0$.

We will now calculate the integral in (2.7). First, we write the integral as the limit of an integral with finite boundaries:

$$v(t) = \lim_{c\to\infty}\int_{-c}^{c} y(\eta,t)L(\eta),$$

with $c\in\mathbb{R}_+$. Next, consider the arc given by $ce^{i\theta}$ for θ from 0 to $-\pi$, which traverses the lower half complex plane. Combined with the interval of integration, i.e. the real line from $-c$ to c, it forms a closed contour in the lower half complex plane, that we define by C. Note that for large enough c, this contour C encloses one pole of $L(\eta)$, namely $\eta_-=\eta_0-i\Delta$. Using the contour, we write

$$\int_{-c}^{c} y(\eta,t)L(\eta)\,d\eta = \int_C y(\eta,t)L(\eta)\,d\eta - \int_{\text{arc}} y(\eta,t)L(\eta)\,d\eta. \tag{2.13}$$

We further assume that $y(\eta,t)$ has no poles in the lower half complex plane. Then, by the residue theorem, the contour integral is equal to minus the residue of the integrand at the single pole of $L(\eta)$ inside the closed contour:

$$\int_C y(\eta,t)L(\eta)\,d\eta = -2\pi i\,\text{Res}(y(\eta,t)L(\eta),\eta_0-i\Delta)$$

$$= -2\pi i(\eta-(\eta_0-i\Delta))y(\eta,t)L(\eta)\Big|_{\eta=\eta_0-i\Delta}$$

$$= y(\eta_0-i\Delta,t).$$

Now, for the arc-integral, we obtain an upper bound:

$$\left| \int_{\text{arc}} y(\eta, t) L(\eta) \, d\eta \right| \leq \pi c \sup_{\text{arc}} |y(\eta, t) L(\eta)| = c\Delta \sup_{\text{arc}} \left| \frac{y(\eta, t)}{(\eta - \eta_0)^2 + \Delta^2} \right|.$$

On the arc we have $|\eta| = c$, so by the reverse triangle inequality:

$$(\eta - \eta_0)^2 = |\eta - \eta_0|^2 \geq ||\eta| - |\eta_0||^2 = |c - |\eta_0||^2 = c^2 - 2c|\eta_0| + |\eta_0|^2,$$

which yields

$$\left| \int_{\text{arc}} y(\eta, t) L(\eta) \, d\eta \right| \leq \sup_{\text{arc}} |y(\eta, t)| \frac{c\Delta}{c^2 - 2c|\eta_0| + |\eta_0|^2 + \Delta^2}.$$

By this upper bound, in the limit $c \to \infty$, the arc-integral goes to zero. If we now consider (2.13) again, take $\lim_{c \to \infty}$ and substitute the results for the contour- and the arc-integral, we obtain:

$$v(t) = \lim_{c \to \infty} \int_{-c}^{c} y(\eta, t) L(\eta) = y(\eta_0 - i\Delta, t).$$

The same argument yields an expression for $r(t)$:

$$r(t) = \frac{1}{\pi\tau} x(\eta_0 - i\Delta, t).$$

Now we combine these and relate them to the complex variable w

$$\pi\tau r(t) + iv(t) = x(\eta_0 - i\Delta, t) + iy(\eta_0 - i\Delta, t) = w(\eta_0 - i\Delta, t).$$

Taking the time-derivative, we obtain:

$$\pi\tau \dot{r}(t) + i\dot{v}(t) = \partial_t w(\eta, t)|_{\eta = \eta_0 - i\Delta} =$$
$$\frac{1}{\tau} \left(-\kappa(\pi\tau r(t) + iv(t)) + i(\eta_0 - i\Delta + Js(t)\tau + \kappa v(t) - (\pi\tau r(t) + iv(t))^2 + I(t)) \right).$$

Splitting the real and imaginary parts yields the final result of this mean-field reduction:

$$\tau \dot{r}(t) = -\kappa r(t) + \frac{\Delta}{\pi\tau} + 2r(t)v(t),$$
$$\tau \dot{v}(t) = (v(t))^2 + \eta_0 + Js(t)\tau + I(t) - (\pi\tau r(t))^2. \tag{2.14}$$

Choosing $Qs(t) = r(t)$ we have a closed system.

2.1.3 Spike-frequency adaptation

Complementing the microscopic model defined by Eqs. (2.1) and (2.2), we introduce a physiological mechanism called spike frequency adaptation (SFA). This is a neuronal fatigue mechanism that depends on the firing rate of an individual neuron. In modelling terms, it is a negative current, of which the value depends on the activity of the neuron. The SFA current of a neuron increases immediately after a spike, before slowly and exponentially decaying again. The situation where, after firing, the SFA current of a neuron has increased, can be interpreted as the specific neuron temporarily having a higher firing threshold. That is, it requires more input before it can fire again. When the neuron remains at rest afterwards, the threshold decreases to its original value. When the timescale of SFA is large relative to the membrane time constant τ, SFA facilitates bursting for appropriate parameter choices [22, 26].

We model SFA as a first-order process with the following differential equation:

$$\tau_A \frac{d}{dt} A_j(t) = -A_j(t) + a \sum_{k, t_j^k < t} \delta(t - t_j^k). \tag{2.15}$$

Here, $A_j(t)$ is the SFA current of neuron j that evolves with a time constant τ_A. The adaptation parameter $a \in \mathbb{R}_+$ defines the amount of increase of $A_j(t)$ after a spike, and in the equation, it is multiplied by the sum of all spikes of neuron j in time. SFA is implemented in the model by adding $-A_j(t)$ to the evolution equation of $V_j(t)$, Eq. (2.1).

For the mean-field reduction to hold after the implementation of SFA, we assume that the mean firing rate of the network approximates the firing rate of each individual neuron. Under that assumption, we approximate the neuron-specific adaptation variable $A_j(t)$ by a global adaptation variable $\bar{A}(t)$, that no longer depends on the spike times of only neuron j, but on the mean firing rate of the total network. The evolution of $\bar{A}(t)$ is given by:

$$\tau_A \frac{d}{dt}\bar{A}(t) = -\bar{A}(t) + \frac{a}{N}\sum_{j=1}^{N}\sum_{k,t_j^k<t}\delta(t-t_j^k), \tag{2.16}$$

and the value of the adaptation variable is equal for all neurons, whence the absence of index j. The applicability of this approximation depends on the differences in incoming current between neurons, since this current determines the firing rate of the individual neuron. These differences are influenced by the parameter Δ, which is the width of the distribution of the heterogeneous input currents $L(\eta)$, defined in Eq. (2.11).

We investigate the effect of the value of Δ on differences between the two SFA implementations by comparing two microscopic models, one with N neuron-specific adaptation variables as in (2.15), and one with a single global adaptation variable as in (2.16). Between these models, we compare the average evolution of the neuron-specific adaptation variables of the former model given by $\langle A\rangle(t) = \frac{1}{N}\sum_j A_j(t)$, to the evolution of the global adaptation variable $\bar{A}(t)$ of the latter. We are interested in the behaviour of the adaptation variables in a bursting regime. The mean adaptation rises fast during the burst, and when it reaches a certain threshold the burst is terminated and the adaptation starts decaying exponentially. Eventually, the adaptation is low enough for a new burst to be initiated. Assuming this general behaviour of adaptation, we derive four features from the pattern of evolution: burst duration, inter-burst interval, minimal adaptation value, and maximal adaptation value. When the relative differences in these features between the two SFA descriptions are < 0.05, we find these descriptions acceptably similar, and thus when we consider the mean-field description including SFA sufficiently comparable to the microscopic model.

When describing the mean-field adaptation, we note that the effect of $\bar{A}(t)$ on the membrane potential is equal to the effect of I. In the mean-field description, we denote the adaptation by $A(t)$. Replacing $I(t)$ by $I(t) - A(t)$ in the mean-field description, and adding the evolution of the mean-field adaptation:

$$\tau_A \frac{d}{dt}A(t) = -A(t) + ar(t), \tag{2.17}$$

incorporates adaptation.

For an overview of all equations of the full system including adaptation, microscopic and mean-field, see Appendix A.1.

2.1.4 Inhibition

We extend the current model of only excitatory neurons to a two-population network of one excitatory and one inhibitory population. Inhibition is relevant in conditions where patients are sedated with propofol, which is often the case in postanoxic coma. The microscopic two-

population model is given by the following equations for $j = 1, ..., N_p$ and for $p \in \{e, i\}$:

$$\tau \dot{V}_j^{(e)} = (V_j^{(e)})^2 + \eta_j^{(e)} + \sum_{p \in \{e,i\}} J_{ep} s_j^{(ep)} \tau_e + \kappa_e g_j^{(e)} + I^{(e)} - A_j^{(e)},$$

$$\tau \dot{V}_j^{(i)} = (V_j^{(i)})^2 + \eta_j^{(i)} + \sum_{p \in \{e,i\}} J_{ip} s_j^{(ip)} \tau_i + \kappa_i g_j^{(i)} + I^{(i)} - A_j^{(i)}, \quad (2.18)$$

$$\text{if } V_j^{(p)} > V_{\text{thr}}, \ V_j^{(p)} \leftarrow V_{\text{reset}},$$

with synaptic dynamics

$$Q_{ab} s_j^{(ab)} = \frac{1}{|S_j^{(ab)}|} \sum_{n \in S_j^{(ab)}} \sum_{k, t_n^k < t} \delta(t - t_n^k), \quad (2.19)$$

with $a, b \in \{e, i\}$ and $Q_{ab} = (1 + \frac{1}{\alpha_{ab}} \frac{d}{dt})^2$. As opposed to the chemical synapses, we only consider gap junctions within a population. The equation for $g_j^{(p)}$ is:

$$g_j^{(p)}(t) = \frac{1}{N_p} \sum_{m \in G_j^{(p)}} (V_m^{(p)}(t) - V_j^{(p)}(t)). \quad (2.20)$$

To conclude the microscopic model, the SFA dynamics for both populations are given by:

$$\tau_A \frac{d}{dt} A_j^{(p)} = -A_j^{(p)} + a_p \sum_{k, t_j^k < t} \delta(t - t_j^k). \quad (2.21)$$

Assuming all-to-all coupling, the above microscopic two-population model also corresponds to a next-generation neural mass model, first derived in [16]. This mean-field model is given by:

$$\tau \dot{r}^{(e)} = -\kappa_e r^{(e)} + \frac{\Delta_e}{\pi \tau} + 2 r^{(e)} v^{(e)},$$

$$\tau \dot{v}^{(e)} = (v^{(e)})^2 + \eta_{0e} + J_{ee} s^{(e)} \tau + J_{ei} s^{(i)} \tau + I^{(e)} - A^{(e)} - (\pi \tau r^{(e)})^2,$$

$$\tau_A \dot{A}^{(e)} = -A^{(e)} + a_e r^{(e)}, \quad (2.22)$$

$$\tau \dot{r}^{(i)} = -\kappa_i r^{(i)} + \frac{\Delta_i}{\pi \tau} + 2 r^{(i)} v^{(i)},$$

$$\tau \dot{v}^{(i)} = (v^{(i)})^2 + \eta_{0i} + J_{ie} s^{(e)} \tau + J_{ii} s^{(i)} \tau + I^{(i)} - (\pi \tau r^{(i)})^2,$$

where the dynamics of $s^{(p)}$ with $p \in \{e, i\}$ are given by $Q_p s^{(p)} = r^{(p)}$ with $Q_p = (1 + \frac{1}{\alpha_p} \frac{d}{dt})^2$.

2.1.5 Network architecture

The exact agreement between the microscopic network model equations and the mean-field model breaks down when, instead of all-to-all, the neurons are sparsely coupled. All-to-all coupling is an essential assumption for the mean-field reduction to hold, it enforces equal synaptic input to all neurons. To find non-identical bursts, which is the goal of this project, we need heterogeneous network behaviour, for which we expect to need more neuron heterogeneity than only induced by η_j. In our network, we introduce variations in synaptic input through sparse synaptic coupling. Neurons are coupled via chemical synapses and gap junctions, and we study sparse coupling of both.

Connections via chemical synapses are unidirectional: an axon of a pre-synaptic neuron connects to the dendritic tree of a post-synaptic neuron, and there is no communication in the opposite direction through the same synapse. A second synapse in the opposite direction, however, is

possible. Chemical synapses can also be self-connections: a neuron's axon connects to its own dendritic tree. In a network of N neurons, all-to-all coupling means that a neuron has N axons, each connected to a different post-synaptic neuron, and there is a total of N^2 synapses. All-to-all coupling, meaning that there is a synapse for every possible neuron-neuron connection, is equivalent to a coupling probability p_{Syn} of 1. We model sparse synaptic coupling by reducing this coupling probability, with steps of 0.1, to a value of 0.1. Examples of random connectivity matrices that correspond to different values of p_{Syn} are shown in Figure 5. In our model equations, the connectivity is embedded in the sets S_j for $j = 1, ..., N$ (see Eq. (2.2)), where each neuron in S_j corresponds to a point in column j in the connectivity matrix. A reduced number of incoming synapses affects the factor $1/|S_j|$ in Eq. (2.2). We approximate this by adjusting J to J/p_{Syn}.

In the two-population model, all-to-all coupling means that every neuron, excitatory and inhibitory, is connected to all other excitatory and inhibitory neurons. When introducing sparse coupling, all synapses exist with a probability of p_{Syn}, like in the one-population model.

Gap junctions provide bidirectional communication between neurons. In the human brain, gap junctions are much sparser than chemical synapses. In modelling studies where sparse occurrence of these junctions was investigated, values between 1 and 4 were chosen for the mean number of gap junctions per neuron [36, 37]. In these experiments, there was no coupling by chemical synapses. We will investigate sparse gap junction coupling for values in the range of these previously chosen coupling probabilities. The gap junction coupling probability is denoted by p_{Gap}.

For the microscopic model, we draw the external background currents η_j from a distribution $L(\eta)$. A specific microscopic network is characterised by its values of η_j. When we simulate different sparsity settings in a specific network, we use the same draw of η_j's for different values of p_{Syn}.

Unless stated otherwise, we use $N = 10000$ in simulations of the microscopic model. For simulations with inhibition, we use $N_e = 8000$ and $N_i = 2000$, according to the ratio used in [38].

2.2 Analysis of bursts in spiking networks

In simulations of bursts, we are interested in the shape of the individual bursts and the similarity between these shapes. When we mention burst shape, we refer to the pattern of $v/\bar{v}$-evolution, the variable of interest since it is an approximation of EEG. We define an algorithm for automated burst detection, visualised in Figure 6. For each burst, we define a suitable burst-threshold by visual inspection, such that in all bursts, the firing rate is above this threshold. Given this burst-threshold, we reduce the time series to a binary sequence, to which we apply a template of the
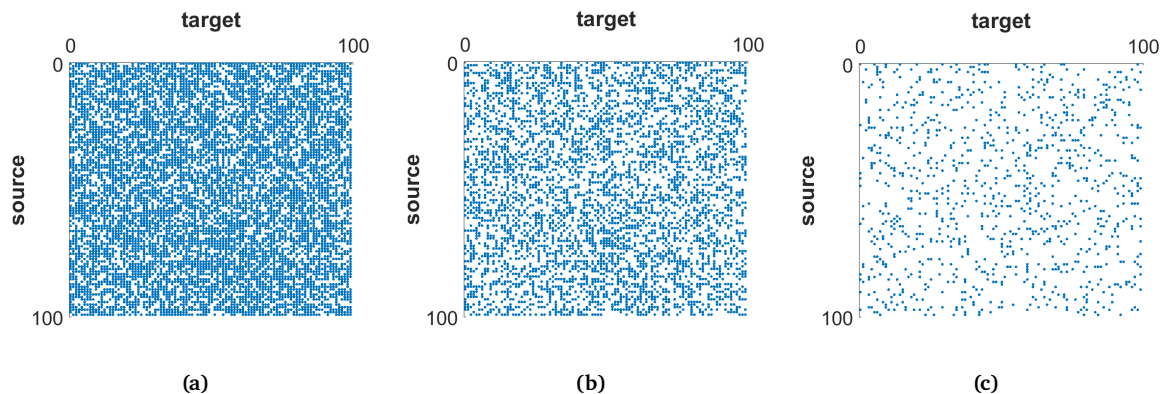

Figure 5: Connectivity matrices of the first 100 neurons in a network for (a) $p_{Syn} = 0.7$, (b) $p_{Syn} = 0.4$, and (c) $p_{Syn} = 0.1$. A point indicates that there is a synaptic connection from the source neuron to the target neuron. Note that the matrices are non-symmetric: a synaptic connection from neuron i to j can, but is not necessarily accompanied by a synaptic connection from neuron j to i.
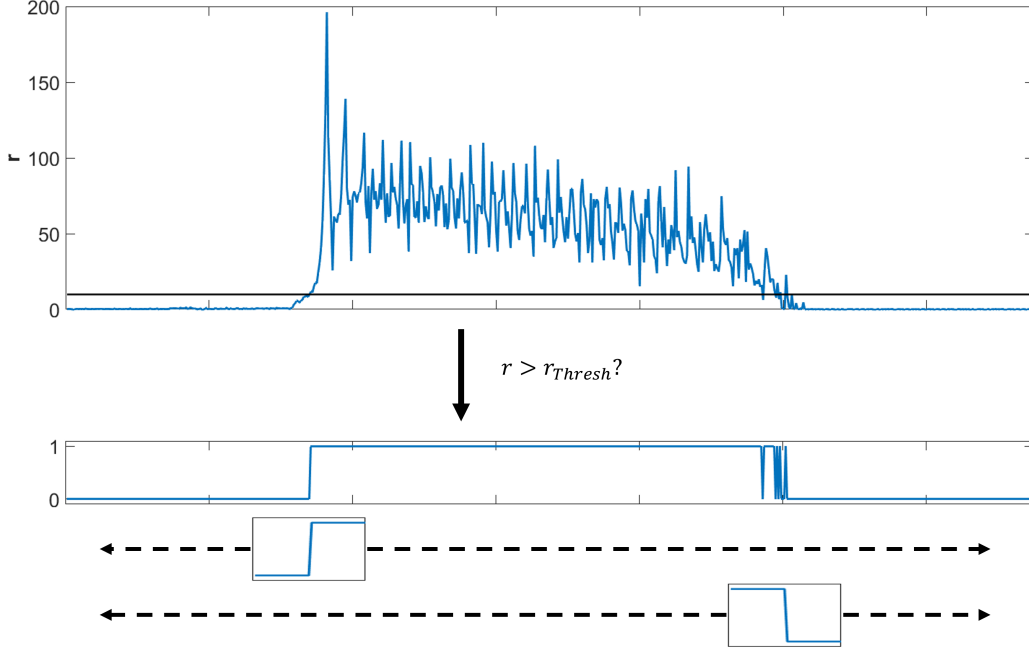
Figure 6: The burst detection algorithm detects bursts in a given time series. First, we extract where the firing rate is above the threshold, i.e. we evaluate $r > r_{Thresh}$. $r_{Thresh} = 10$ is visualised in the top plot. The result is the r evolution represented by 0's and 1's. We shift two templates over this binary representation, one template for burst onset and one template for burst termination. The locations where the absolute differences between the binary representation and the onset and termination template have extrema are marked as burst onset and termination, respectively. This shows an example for a short epoch that already contains a burst, but the algorithm can be applied to a complete time series at once, detecting multiple bursts simultaneously.

form $(0, ..., 0, 1, ..., 1)$, where we denote the number of 0's and 1's by n_{01}. The time-shift for a good fit of the template on the binary representation of the simulation corresponds to the onset of a burst. A flipped version of the template is used for the detection of burst termination.

After detecting the bursts, we analyse their shape by measuring the similarity of burst shapes within one simulation. As a measure for burst similarity, we compute the cross-correlation of the different bursts, following previous research on burst-suppression with (non-)identical bursts [3]. We denote the ith of n bursts of a simulation by B_i, with $i \in I_B$ where $I_B = \{1, ..., n\}$. We denote the burst similarity within a simulation by q, defined as:

$$q = \frac{\sum_{i \in I_B} \sum_{j \in I_B \setminus \{i\}} \max(\text{NCC}(B_i, B_j))}{n(n-1)}, \tag{2.23}$$

where, $\text{NCC}(X, Y)$ is the normalised cross-correlation between time series X and Y. In words: the burst similarity within a simulation is calculated as the mean of the maxima of the normalised cross-correlations between all individual bursts (auto-correlations excluded).

We want to distinguish between BS with identical and non-identical bursts, and define the following: a simulation is classified as BSNIB when the burst similarity is below 0.75, and BSIB when it is above 0.75. These values are consistent with [3].

2.3 Comparison of simulations and EEG

A qualitative comparison of simulations and clinical EEGs is outside the scope of this project. The EEGs, however, are the main motivation for this project, and therefore we will provide a short, non-empirical evaluation of the similarity of visually observable features in simulations and EEG. Since we can not study channel synchrony in our one- and two-population models, we

only compare the burst onset and burst progression pattern of our simulations with the EEGs in Figure 1.

2.4 Computational methods

With bifurcation analysis of the mean-field model, we find parameter regions where the model exhibits bursting behaviour. We use the bifurcation analysis software MatCont (version 7p4) [39] for all bifurcation diagrams.

For simulations of the mean-field model and the microscopic model, we wrote custom code in Python using the Brian2 package [40]. The mean-field model is implemented in Brian2 as one NeuronGroup with a single neuron, described by the mean-field equations (2.14). To implement the microscopic network, we transform it into a network of coupled θ oscillators. Each neuron is described by its phase variable θ_j through the transformation $V_j = \tan\left(\frac{\theta_j}{2}\right)$. Hereby $V_j \in [-\infty, \infty]$ transforms to $\theta_j \in [-\pi, \pi]$, and the threshold-reset rule changes to a continuous trajectory on the unit circle since $\pi = -\pi \mod 2\pi$. For implementation in Brian2, the transformation yields a change of the threshold value to $\theta_{\text{thr}} = \pi$ and the reset value to $\theta_{\text{reset}} = -\pi$. Using a different approach following [18], we also performed a mean-field reduction of this network of θ oscillators, which can be consulted in Appendix A.2. In the end, we are interested in the evolution of the mean membrane potential of the network, since we can relate this to simulations of the mean-field model, as well as to EEG. Therefore, at each time step, we transform each θ_j back to V_j and compute $\bar{v} = \frac{1}{N} \sum_{j=1}^{N} V_j$, to obtain the evolution of the mean membrane potential. We prevent extremely large peaks in V_j by applying a corrected transformation $V_j = \tan\left(\frac{\theta_j}{2+\varepsilon}\right)$, where $\varepsilon = 0.05$.

We must account for one possible singularity in the θ-evolution equation. Each time a neuron with a gap junction spikes and is then reset to $\theta_j = -\pi$, a denominator of the gap junction connection term of the connected neuron equals zero, see Eq. A.5. We prevent this singularity by adding ε_2 to the denominator which then becomes $1 + \cos\theta_m + \varepsilon_2$, where we set $\varepsilon_2 = 0.01$.

For noise in Brian2, we use the predefined Gaussian random variable ξ with mean 0 and standard deviation 1. In our microscopic model description with θ-variable, we replace I_j by $I_j + \sigma\xi$ in the θ-evolution equation, where σ is the desired standard deviation of the noise. This is an individual noise term, each neuron receives independent noise.

For numerical integration without noise, we use the built-in Brian2 RK4 method with fixed step-size. With noise, we choose the Brian2 built-in stochastic Heun method, because additive noise in the V-description translates to multiplicative noise in the θ-description.

Each simulation has a duration of 50 seconds, from which we discard the first 10 seconds of transients. Unless stated otherwise, all state variables are initialised at 0.

3 Results

First, we identify parameter regions where we find bursting behaviour. Then, as the main result, we analyse simulations that show bursting behaviour.

3.1 Model behaviour exploration

We present here an example of a bursting regime in the microscopic model and the neural mass model, and explore the dependence of burst characteristics on parameter settings for SFA and gap junction coupling. We investigate sparse gap junction coupling, but remain at all-to-all coupling via chemical synapses in this section. By analysing the neural mass model, we identify parameter regimes for bursting, which we later use for simulations of the microscopic model.

3.1.1 Mean-field and microscopic burster

With parameter settings as in Table 1, the mean-field model defined by Eqs. (A.4) is a fold-fold burster (see Section 1.3 and [28]). Note that $\tau_A \gg \tau$, whereby the evolution of A forms a slow subsystem, and the dynamics of r, v and s form a fast subsystem. The rest state of the identified fold-fold burster is given by a branch of stable nodes, and damped oscillations near a branch of stable foci account for the active state. A bursting solution superimposed on the underlying bifurcation structure of the fast subsystem is visualised in Figure 7, with slow variable A as the bifurcation constant. The value of A determines the number of equilibria. There is only one for $A < 0.60$ (a stable focus) and $A > 2.12$ (a stable node), whereas there are three for $0.60 < A < 2.12$ (a stable focus, a saddle and a stable node). By the evolution of A, the fixed point structure of the fast subsystem varies. The manifold $G = \{(v, r) : \dot{A} = 0\}$ divides the phase space into a region where $\dot{A} < 0$, which is below G, and a region where $\dot{A} > 0$, above G. The position of G for these parameter settings is shown in Figure 8a. Note that G is independent of v.

Assuming that any damped oscillations around the stable focus are confined to a neighbourhood N_U above G, the full system has a periodic bursting solution, and it is reached for any initial condition.

The reasoning behind this statement is visualised in Figure 8. First, we define additional neighbourhoods N_L surrounding the stable node equilibrium, N_{FL} surrounding the lower fold bifurcation, and N_{FU} surrounding the upper fold bifurcation. Here we note that N_{FU} lies above G, N_L and N_{FL} lie below it. For any initial A, there is at least one stable equilibrium in the fast

Table 1: Parameter values for the burster in Figure 7. We use the same parameter values for simulations of the microscopic model. Note that only time-related parameters have a unit, all other parameters are unitless.

| Symbol	Value	Unit	Parameter description
τ	10	ms	membrane time constant
α	1/2	ms^{-1}	synaptic rise/decay rate
k	0	-	gap junction coupling strength
J	8	-	synaptic coupling strength
Δ	0.01	-	external heterogeneous current distribution HWHM
η_0	0.5	-	external heterogeneous current distribution center
I	0	-	time-varying input current
τ_A	5000	ms	adaptation time constant
a	0.5	-	adaptation parameter
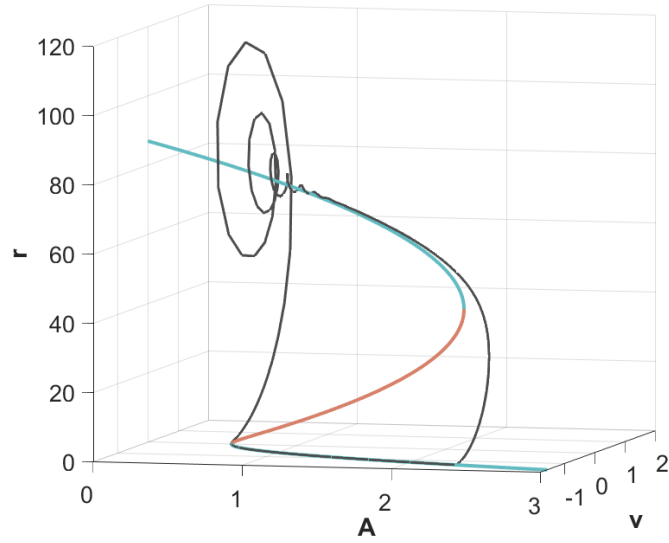
Figure 7: A bursting solution of the mean-field model superimposed on the bifurcation diagram with slow variable A as parameter. The direction of the simulation is clockwise. This type of burster is called a fold-fold burster, because the bifurcations of the rest state and the active state are both fold bifurcations. The rest state of this burster is located at the branch of stable nodes around $r = 0$, and with values of v between -2 and 0. At the fold bifurcation of the rest state at $A = 0.60$, the solution jumps to the branch of stable foci, initiating a burst. The active state behaviour of this burster is given by damped oscillations around the equilibrium branch. Moving right along the branch, the solution reaches the fold bifurcation of the active state, which terminates the burst. The rest state is reached, starting a new cycle. Parameter values as in Table 1.
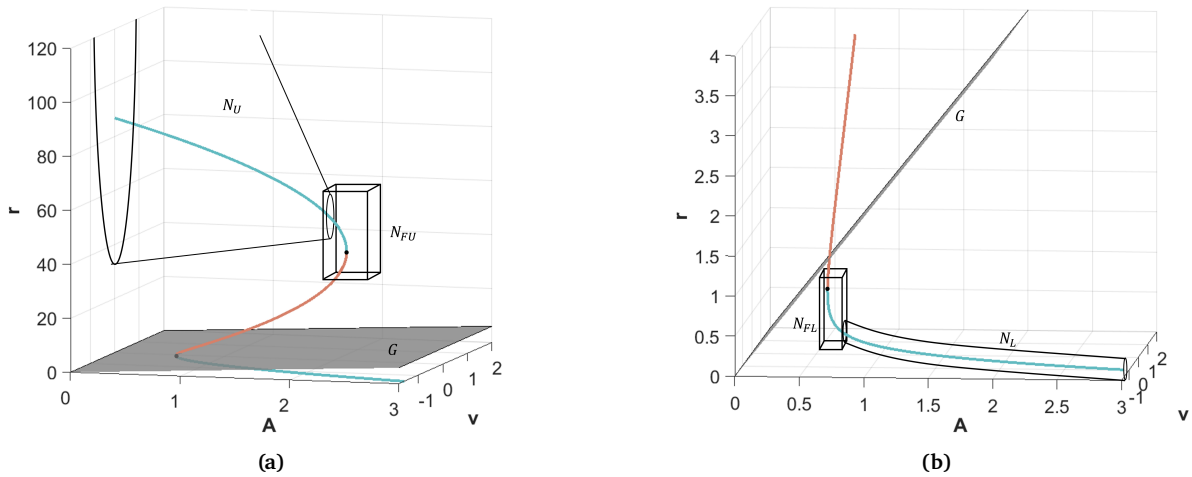

(a)

(b)

Figure 8: The bifurcation diagram for the burster in Figure 7 with neighbourhoods N_U, N_{FU}, N_L and N_{FL} surrounding the stable equilibrium branches and the fold bifurcation points. In (a), we show the full bifurcation curve for $0 < A < 3$, focusing on the branch of stable foci, which is the active state for this burster. On manifold G, we have $\dot{A} = 0$, above G we have $\dot{A} > 0$. N_U is the neighbourhood where be assume the damped oscillations around the branch of stable foci are restricted to. N_{FU} defines the neighbourhood of the right fold bifurcation, the bifurcation of the active state. We zoom into the bottom of this figure to arrive at (b). The manifold G is the same as in (b). N_L is the neighbourhood around the branch of stable nodes. N_{FU} defines the neighbourhood of the left fold bifurcation, the bifurcation of the rest state.
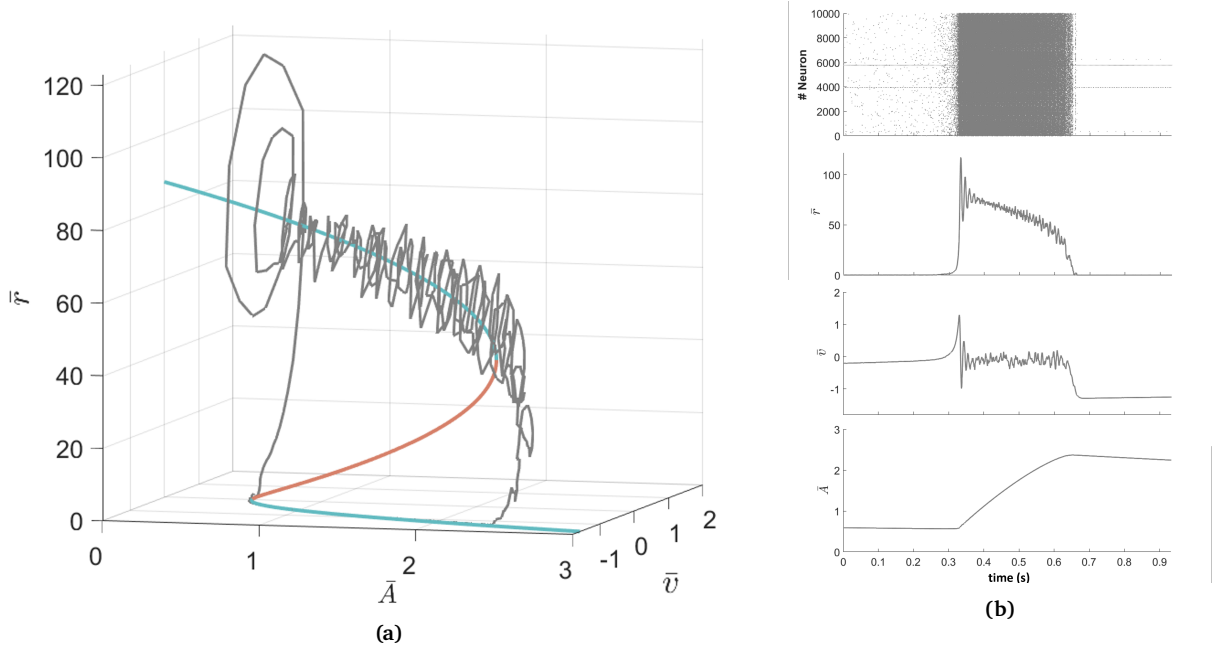
19

Figure 9: A burster similar to the one in Figure 7, but now in the microscopic model. In (a) we show the bursting solution superimposed on the bifurcation structure of the mean-field model. This bursting solution also follows the trajectories defined for the mean-field burster. In (b), we show a rasterplot of the burst, and the evolution of r, v and A during the burst over time.

subsystem, so every initial coordinate lies in the basin of attraction of either the stable focus, or the stable node. Considering $\tau_A \gg \tau$, the fixed point structure and basin(s) of attraction do not change before the solution reaches N_L or N_U. We now describe two trajectories. Trajectory 1: the solution is at N_L, which is below G and therefore $\dot{A} < 0$. The solution must follow N_L, reaches N_{FL} where still $\dot{A} < 0$, and then escapes N_{FL} as the lower fold bifurcation is passed. The only attractor that now remains is the stable focus, and the solution reaches N_U. We now continue with trajectory 2: the solution is at N_U, which is above G and therefore $\dot{A} > 0$. The solution follows N_U, and reaches N_{FU} where still $\dot{A} > 0$. It passes the fold bifurcation, such that the only attractor that remains is the stable node, and the solution reaches N_L. This shows that the only possible solution follows an alternating sequence of trajectories 1 and 2, which defines a periodic bursting solution.

Returning to the bursting solution in Figure 8b, we see that it precisely follows the described trajectories. As expected from the exact match between the mean-field model and the microscopic model, this burster also exists in the microscopic model. A simulation of the microscopic model that shows bursting is visualised in Figure 9, again superimposed on the bifurcation structure to show the exact agreement with the mean-field model. Figure 10 shows how A evolves over multiple bursts.

3.1.2 Approximation of individual SFA

We evaluated the differences between the neuron-individual SFA description (Eq. 2.15) and the population SFA description (Eq. 2.16) incorporated in the microscopic model for $\Delta \in \{0.001, 0.002, 0.005, 0.01, 0.02, 0.05\}$. The relative differences of the features between the two descriptions are plotted against Δ in Figure 11, beside examples of the evolution of $\langle A \rangle(t)$ and $\bar{A}(t)$ in time for $\Delta = 0.001, 0.1$. The global pattern of evolution is similar for both depicted values of Δ, however, especially the inter-burst interval shows considerable variation between the two SFA descriptions, and this variation grows with Δ.
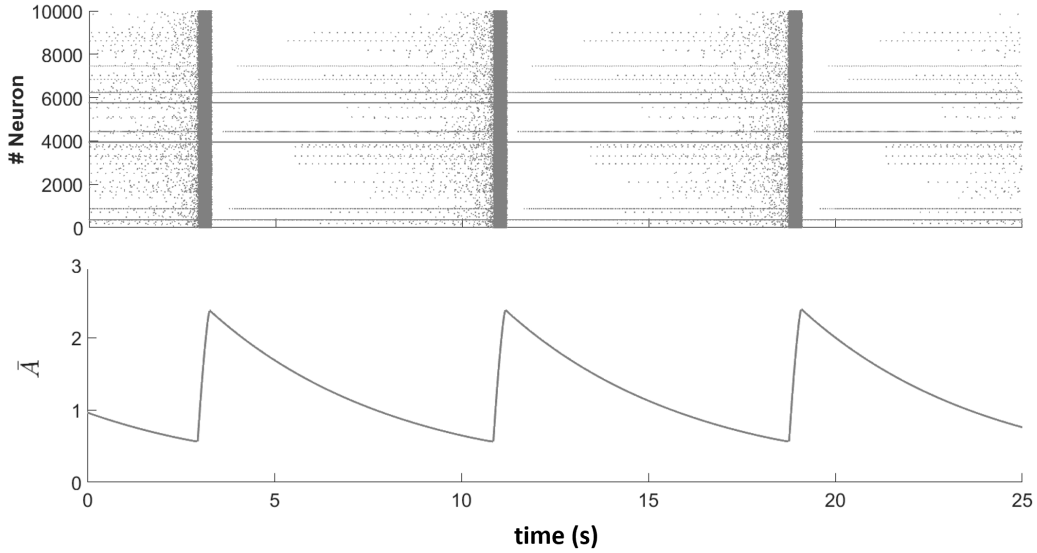
Figure 10: A rasterplot and the evolution of $\bar{A}$ for a simulation of 25 s duration, showing three bursts. During a burst, $\bar{A}$ rises, and in between bursts it exponentially decays.

3.1.3 Effect of gap junctions

First, we investigated the effect of the gap junction strength κ on the behaviour of the model in terms of the bifurcation structure of the fast subsystem. Given $\Delta = 0.01$, we computed bifurcation diagrams in parameters η_0 and $J > 0$, for $\kappa \in \{0, 0.25, 0.5, 0.75, 1, 1.2\}$. The computed curves of Fold and Hopf bifurcations are visualised in Figure 12. The curves of fold bifurcations are very similar between different κ settings, only the course of the left branch, the disappearance of the high-activity stable equilibrium state, changes slightly. The course of the curve of Hopf bifurcations, however, depends strongly on κ. For $\kappa = 0$, i.e. absence of gap junctions, no Hopf bifurcations occur for $J > 0$. For $\kappa > 0$, a branch of Hopf bifurcations emerges from a
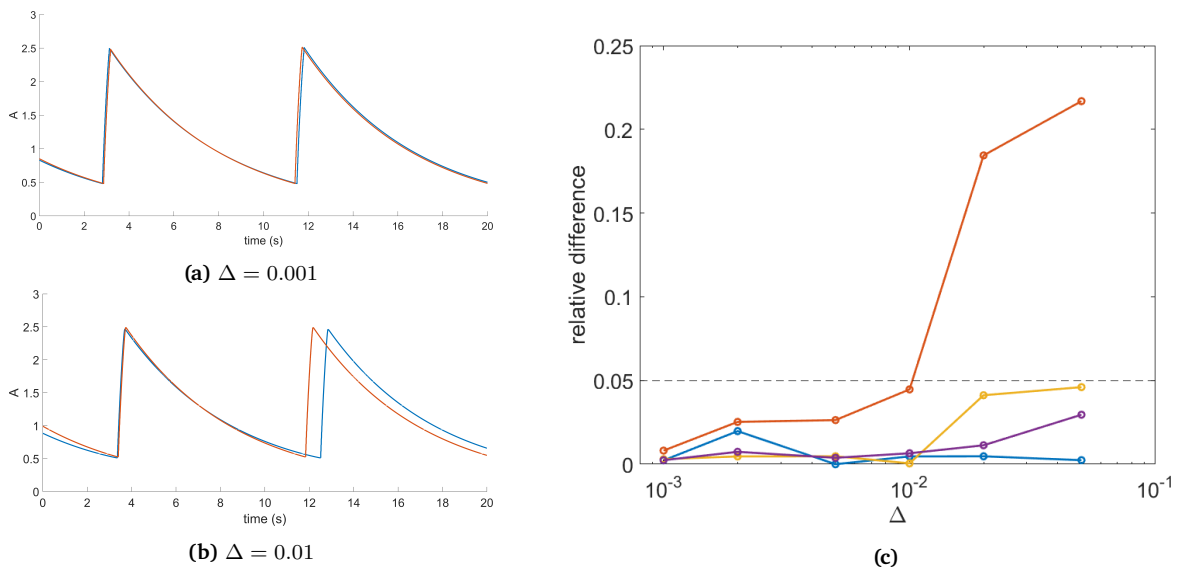

(a) $\Delta = 0.001$

(b) $\Delta = 0.01$

(c)

Figure 11: As Δ is increased, the differences between the individual and the global adaptation description grow. (a) and (b) show time traces of the individual (red) and the global (blue) adaptation description. The value $\Delta = 0.01$ is the largest where the relative difference of the adaptation features between both descriptions stays below 0.05. In (c), the relative differences in the burst duration (blue), inter-burst-interval (red), minimal value of A (yellow) and maximal value of A (purple) are shown for $\Delta = 0.001, 0.002, 0.005, 0.01, 0.02, 0.05$. The relative difference in inter-burst-interval is the largest of all features for all considered values of Δ.
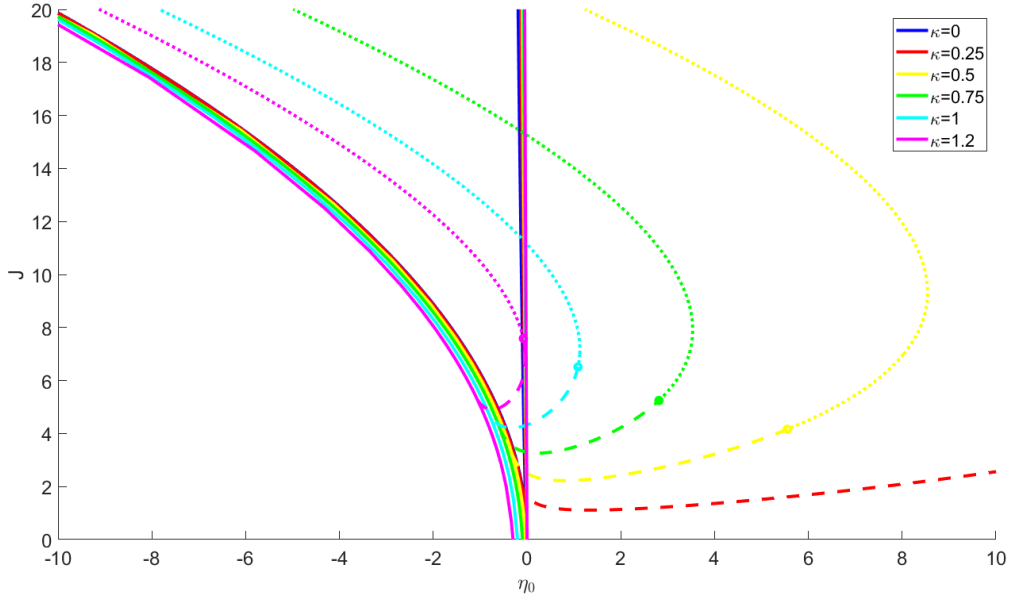
Figure 12: Bifurcation curves of the mean-field model for values of κ between 0 and 1.2. The solid curves are branches of fold bifurcations, dashed and dotted curves are branches of super- and subcritical Hopf bifurcations, respectively. The transitions of supercritical to subcritical Hopf bifurcation occur at Bautin bifurcations, which are visualised as circles. For each value of κ, the two branches of fold bifurcations collide in a Cusp point. These are not highlighted in this figure.

Bogdanov-Takens bifurcation on the left fold bifurcation branch, and this Hopf branch moves left as κ increases. For $\kappa \geq 1.2$, the Hopf curve does not cross the right fold bifurcation branch. With all current parameter settings, the Hopf point occurs at the high-activity equilibrium. From the Bogdanov-Takens bifurcation, also a small branch of homoclinic bifurcations emerges, which is not shown.

Toward a more realistic network architecture, we analysed simulations of a network with very sparse gap junction coupling. The coupling strength was set to $\kappa = 1.2$, expecting the occurrence of a Hopf bifurcation of the high-activity equilibrium within the parameter range of interest. Figure 13 shows a simulation of the microscopic model with all-to-all gap junction coupling and one with a sparse gap junction coupling of 3 gap junctions per neuron on average, which is approximately a 3000-fold reduction in the number of junctions. All-to-all gap junction coupling results in large oscillations at the start of a burst, with much higher amplitudes than in the sparse coupling case.

It is more relevant to evaluate whether these sparse gap junctions still have an observable effect as opposed to no gap junction coupling. We investigated both cases for different synaptic coupling probabilities. Representative bursts for both settings and for $p_{syn} = 1, 0.7, 0.4$ are shown in Figure 14. For all p_{Syn}, the burst pattern is highly similar between the two considered gap junction settings. The single minor difference is a shift in $\bar{v}$.

3.1.4 Model parameters for bursting

Considering the negligible effect of gap junctions with a realistic number of juntions, we continue the analysis with $\kappa = 0$ and $p_{gap} = 0$. In the fast subsystem, external inputs to the neurons are now provided by synaptic input, regulated by J, and the constant external current, η_j. This second term, η_j, is drawn from a distribution defined by parameters η_0 and Δ. The effect of the parameters J, η_0, and Δ on the bifurcation structure of the fast subsystem is visualised in Figure 15. The bifurcation diagram for $\Delta = 0.01$ is visualised in magenta, whereas diagrams for $\Delta = 0.02, 0.05, 0.1, 0.2, 0.5, 1, 2$ are visualised in grey. For all values of Δ, we see two branches
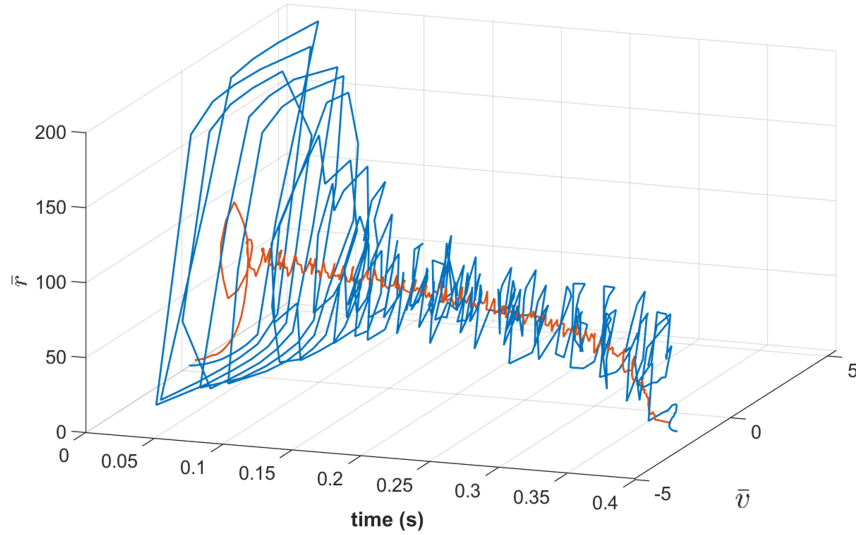
Figure 13: Two simulations of the microscopic model, with $p_{Gap} = 1$ in blue, and $p_{Gap} = 3/N$ in orange. The $\bar{r}$ and $\bar{v}$ evolution is shown over time. The simulation with full gap junction coupling shows very large oscillations. When p_{Gap} is reduced, these oscillations are substantially smaller.

(a) $p_{Syn} = 1$ **(b)** $p_{Syn} = 0.7$ **(c)** $p_{Syn} = 0.4$
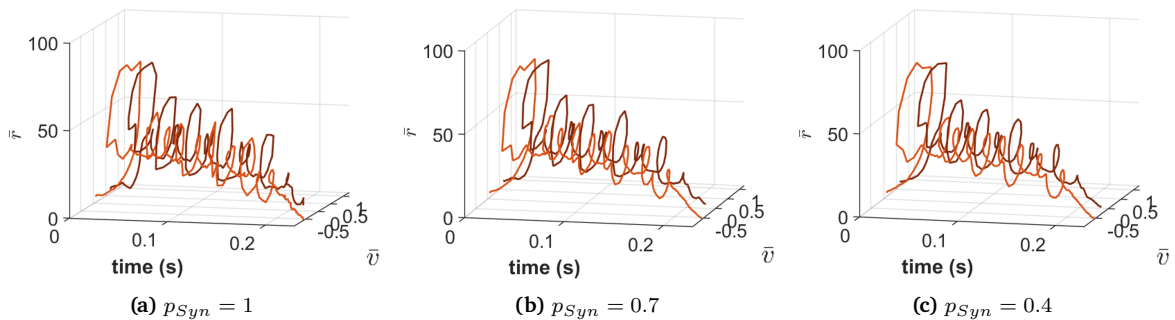
Figure 14: Simulations showing the effect of removing the gap junctions (orange curves), compared to sparse gap junction coupling with $p_{Gap} = 3/N$ (red curves), for $p_{Syn} = 1, 0.7, 0.4$. The evolution of $\bar{r}$ and $\bar{v}$ is shown over time. The value of $\bar{v}$ differs between the two gap junction settings, but the burst pattern is highly similar. A single difference from the parameter settings for Figure 13 is that here, $J = 4$.
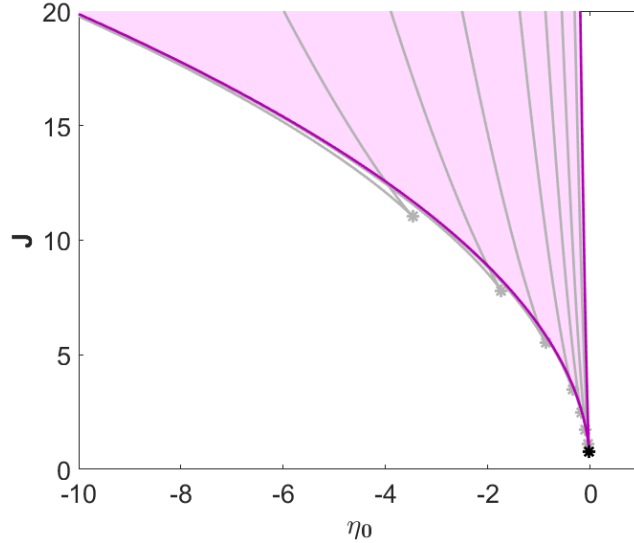
23

Figure 15: Bifurcation diagram of the mean-field model with no gap junction coupling, i.e. $\kappa = 0$. Bifurcation parameters are J, the gap junction coupling strength, and η_0, the center of the distribution of external background currents. The diagram for $\Delta = 0.01$ is shown in magenta. As Δ is increased up to 2, the bifurcation diagram moves left and up, shown in grey. Cusp points are identified with a star.

of fold bifurcations that collide in a Cusp point. A region of bistability lies in between these two branches, the magenta-shaded region shows the bistability region for $\Delta = 0.01$. A critical condition for finding a fold-fold burster after adding SFA is $J > J_{Cusp}$, i.e. the parameter choice allows a bistable regime. When Δ is increased, the cusp point moves up, and larger synaptic connection strengths J are needed for a bistability region. Note that effectively, variation of A induces movement along the η_0-axis.

3.2 Sparse synaptic coupling

As opposed to the above, we introduce sparse synaptic coupling here. This means that exact agreement between the microscopic and mean-field model breaks down, and we investigate what heterogeneous behaviour results from this intervention.

The parameters used for simulations of the microscopic model with reduced synaptic coupling probabilities are the same as in Table 1, except for the synaptic coupling strength, which is now $J = 4$. We experimented with p_{Syn} between 1 and 0.1 with steps of 0.1 for 10 different networks, i.e. 10 different realisations of random sparse synapses and random η_j drawn from $L(\eta)$. For a specific network, each choice of p_{Syn} yields a simulation, and from each simulation we compute one burst similarity value q. These values for all experiments are summarised in Figure 16. It shows that for $p_{Syn} > 0.8$, q remains below the threshold for identical bursts. The bursts within a simulation become more identical when p_{Syn} is decreased.

Using Eq. (2.23), each value of q is computed as the mean of $N_B^2 - N_B$ cross-correlation values, where N_B is the number of bursts in the simulation. All simulations with $p_{Syn} = 1$ have a bimodal distribution of these cross-correlation values, indicating two groups of bursts with a high within-group burst similarity and a low similarity between the groups. This distribution is shown for one simulation with $p_{Syn} = 1$ in Figure 20a, with peaks at 0.6 and 0.8. The burst shapes that cause these values are visualised in Figure 17, where we show four consecutive bursts in a representative simulation with $p_{Syn} = 1$. The first and third highlighted bursts have a cross-correlation of 0.88, and the second and fourth highlighted bursts have a cross-correlation of 0.77, whereas the mean of the cross-correlations between the remaining burst combinations is only 0.57. This means that the simulation is an alternation of bursts from two groups of similar bursts. This alternating
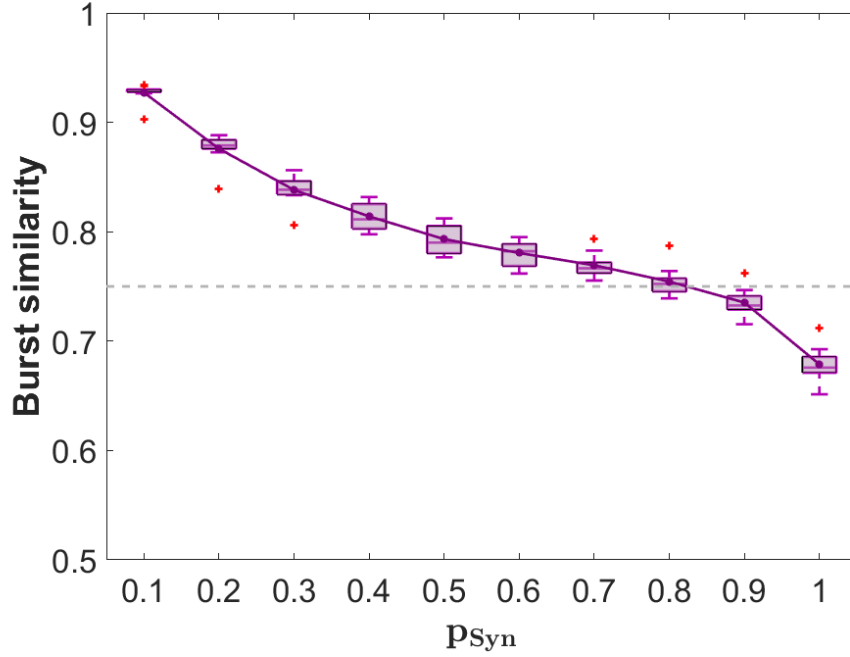
24

Figure 16: Mean values of burst similarity for ten different networks, for different synaptic coupling probabilities p_{Syn}. The threshold for identical bursts is considered $q = 0.75$, shown as a dashed grey line. Connected purple points show the mean values of q of ten different networks for a given p_{Syn}, the purple boxes show the median and quartiles. Outliers are visualised as red crosses. For $p_{Syn} > 0.8$, the mean values of q are below the threshold for identical bursts. In all simulations, parameters where as in Table 1, except $J = 4$.

pattern exists for the complete duration of the simulation.

For insight into the individual contribution of neurons to the specific burst shapes, we show the spiking pattern that corresponds to two highlighted bursts in Figure 18. Note that, by the spiking behaviour of a QIF-neuron (see Section 1.2.1), a peak in $\bar{v}$ likely precedes a moment of synchronised spiking activity, which is then followed by a dip in $\bar{v}$. Peaks in $\bar{v}$ thus correspond to groups of neurons spiking simultaneously, so the shape of the $\bar{v}$-evolution, i.e. the burst shape, is largely determined by groups of synchronised neurons. At the bottom of Figure 18, ordering the neurons based on η_j reveals these groups. In the first highlighted burst, the groups denoted by 1 and 3 synchronise, but not the larger group 2. Conversely, in the second highlighted burst, group 2 is highly synchronised, mostly at the start of the burst. The synchronisation of this large group is reflected in the $\bar{v}$-pattern by a large peak, where the second highlighted burst in Figure 18 corresponds to the third highlighted burst in Figure 17.

Another remarkable observation from Figure 18 is that group 2 is active at burst onset in the first burst, whereas in the second burst, group 3 shows burst onset activity. The group that is inactive at burst onset, is responsible for the initial and largest synchronised activity. The group that quits spiking first in the previous burst, is also the first to start spiking at the onset of the subsequent burst.

Ordering the neurons by η_j reveals a pattern of synchronised groups. The distinction between these groups is caused by the neuron-specific SFA variable A_j, as shown in Figure 19. The top shows the same bursts as in Figure 18 but with groups 2 and 3 highlighted. The mean A_j of both groups shows an alternating pattern, where the group spiking last in the first burst, is also last to start spiking in the second burst. These neurons emit one less spike in this second burst, gaining an advantage in A_j for the subsequent burst. The clear distinction in $\bar{A}$-pattern between subgroups of neurons shows that the individual A_j is not accurately approximated by $\bar{A}$.
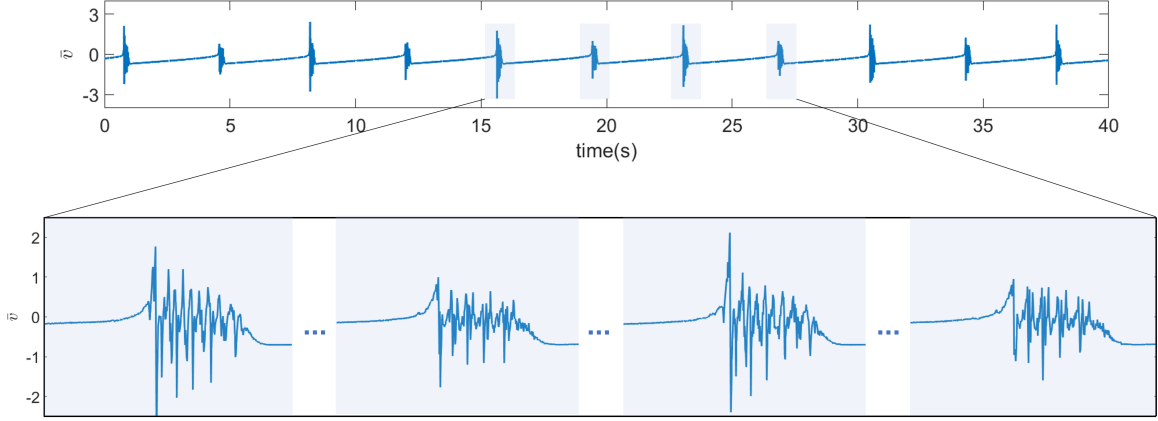
Figure 17: At the top, we show the $\bar{v}$-evolution in one simulation of 40 second duration, where $p_{Syn} = 1$, $J = 4$, and the other parameters as in Table 1. The fifth to eighth bursts are highlighted, and shown at the bottom. The fifth and seventh bursts are similar, with a cross-correlation of 0.88, and also the sixth and eighth bursts are similar, with a cross-correlation of 0.77. The mean cross-correlations between both groups is 0.57.

Reducing the synaptic coupling probability from $p_{Syn} = 1$, the distribution of cross-correlations between bursts remains bimodal until $p_{Syn} = 0.6$. This distribution for $p_{Syn} = 0.6$ is shown in Figure 20b, with peaks at 0.7 and 0.9. The two separate peaks still suggest two similarity groups, but both peaks have moved to higher values of cross-correlation, indicating both a higher between-group similarity and a higher within-group similarity. Four representative bursts are shown in Figure S1a.

With $p_{Syn} = 0.1$, bursts become more similar, we can no longer distinguish between two groups in the histogram in Figure 20c. The bursts are highly similar, the burst similarity value between each pair of bursts is higher than 0.9. Sparse synaptic coupling causes more difference in synaptic input between neurons, which reduces the effect of individual SFA. Four representative bursts for $p_{Syn} = 0.1$ are shown in Figure S1b.

3.3   Individual additive noise

Adding individual noise to each neuron causes the firing rate of each neuron to be less regular. Increasing the standard deviation of the noise reduces synchronisation between neurons, as shown in Figure 21. Note that for $\sigma = 0.01$, the standard deviation of the noise equals the HWHM of the distribution of η. For high levels of noise, the burst is only an epoch of overall higher activity, there is no pattern with peaks and dips, which is more naturally observed in bursts. Bursts with intermediate values of σ are visualised in Figure S2. With $\sigma = 0.5$ and higher, no bursts can be observed, there is only sustained asynchronous activity.

3.4   Bursting with inhibition

For simulations with inhibition, we used parameter settings comparable to the simulations with only excitation, the settings are shown in Table 2. We distinguish two modes: one with low intrinsic inhibitory activity where $\eta_{0i} < 0$, and one with high intrinsic inhibitory activity where $\eta_{0i} > 0$.

In the mode with low inhibitory activity, values of q for different p_{Syn} are comparable to those of the simulations with only excitation, shown in Figure S3. The inhibitory neurons are synchronised with the excitatory neurons, following the same bursting pattern, see Figure 22a. Shapes of the bursts and the underlying spiking structure for three consecutive bursts in a simulation with $p_{Syn} = 1$ are shown in Figure 23. The burst shapes show comparable peak timing, but are
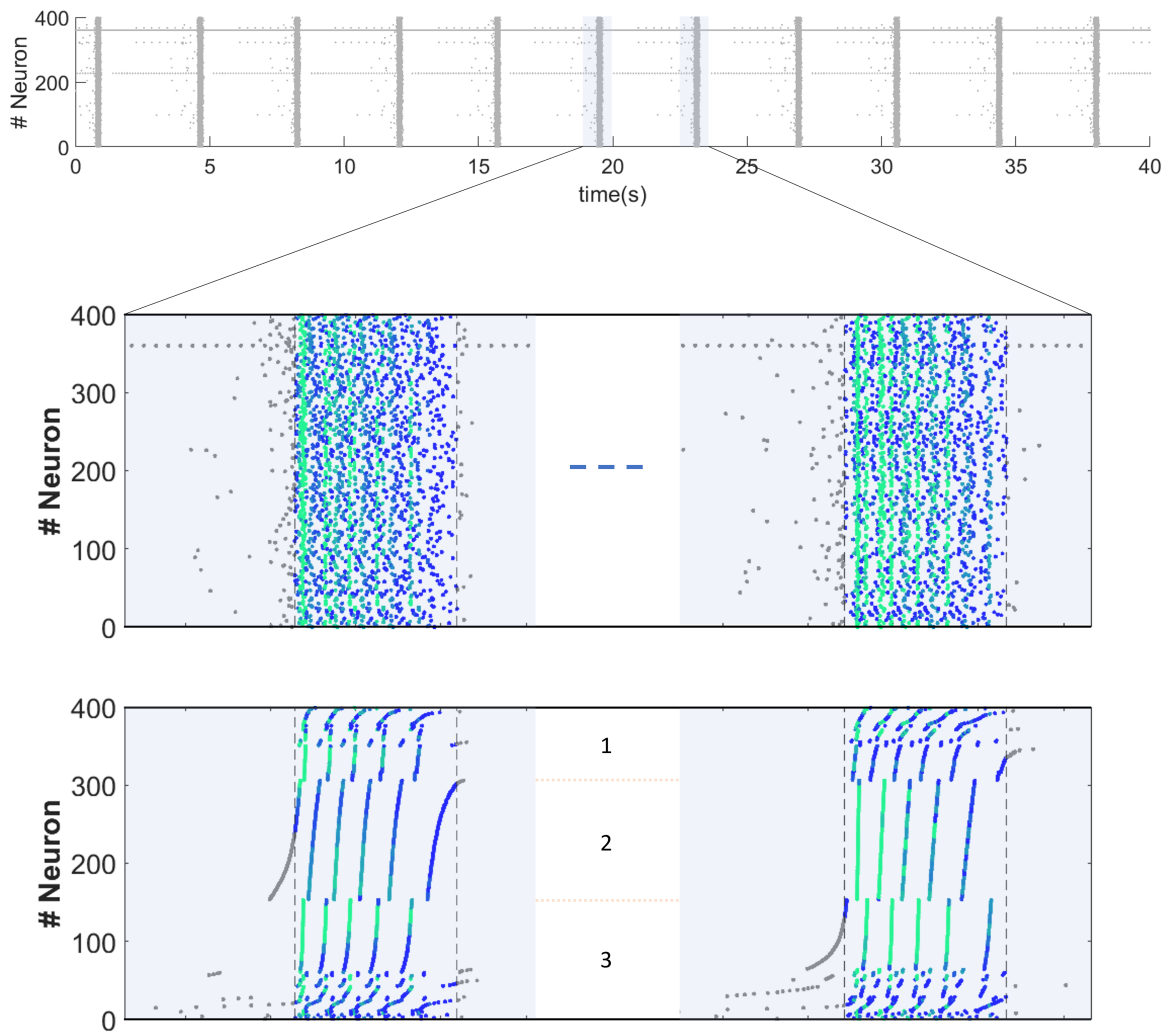
26

Figure 18: The top raster plot shows the same burst as in Figure 17. The sixth and seventh bursts are highlighted. of the 10000 neurons in total, we selected 400 based on their value of η. Each point denotes a spike. The colour of the points is based on the firing rate of the network at that time. Green shows a high firing rate, blue a lower firing rate. In the bottom raster plot, we order the neurons based on η, where neurons with highest η have a low index, and values of η decrease with increasing index. Vertical dashed lines show burst onset and termination, as determined by the burst detection algorithm. The numbers 1, 2 and 3 in the bottom raster plot divide the neurons into groups, where the borders are evident from the ordered raster plots.
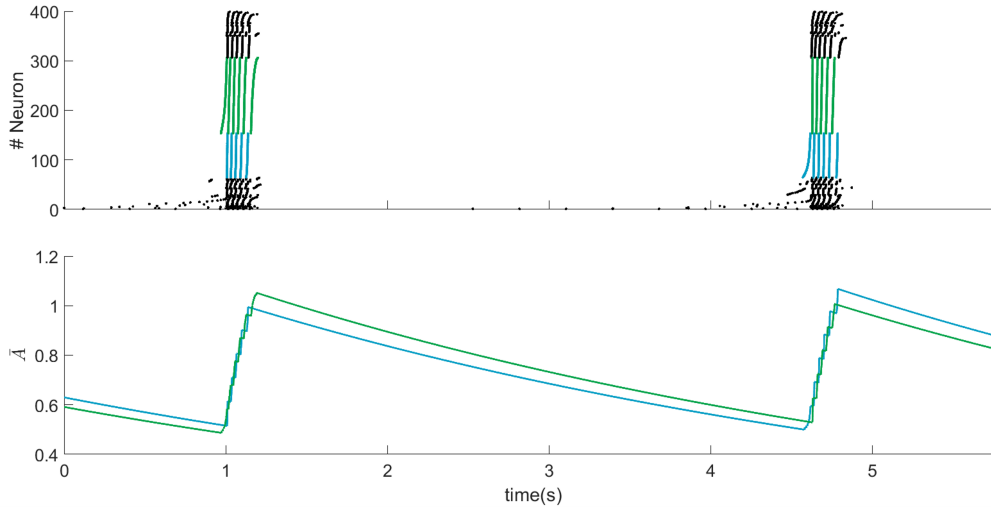
Figure 19: At the top: a raster plot of the same two bursts as in Figure 18, where group 2 and 3 as depicted there, are shown here in green and blue, respectively. From each group, we selected 11 neurons and recorded their A_j evolution. The mean for each group is graphed at the bottom in the corresponding colour. There is an alternating pattern between which group spikes at burst onset and also at burst termination. This is also seen in the $\bar{A}$-evolution of both groups.
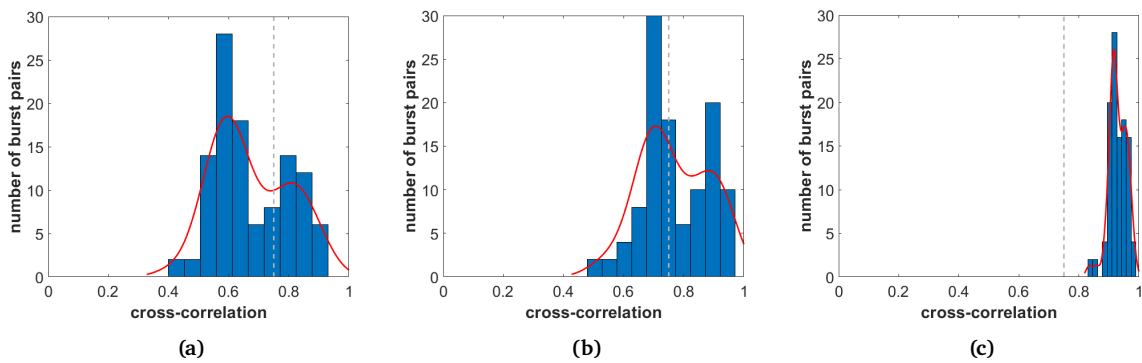

Figure 20: Distribution of the cross-correlations between bursts in simulations with (a) $p_{Syn} = 1$, (b) $p_{Syn} = 0.6$, and (c) $p_{Syn} = 0.1$. The red curves are matlab-fitted nonparametric kernel-smoothing distributions.

still very dissimilar. The raster plots show again distinctive SFA-induced synchronised groups of neurons.

High intrinsic inhibitory activity causes sustained spiking of the inhibitory neurons, also during the inter-burst-intervals, see Figure 22b. The values of q for simulations in this mode remain below the threshold of 0.75 until $p_{Syn} = 0.2$, as shown in Figure 24. Burst shapes and spiking patterns of three consecutive bursts from a simulation with $p_{Syn} = 1$ are shown in Figure 25. The burst shapes reveal that the rest state has become an oscillatory state with small amplitude oscillations. The peak at burst onset in the second burst is smaller than in the other two bursts, and also than other bursts we showed in our results. As in all other bursts in simulations with $p_{Syn} = 1$, the raster plots show distinctive SFA-induced spiking groups of neurons.

The bursting behaviour in the high activity mode is qualitatively different from that in the low activity mode, which is clear from the simulations of the neural mass model in both modes in Figure 26. Orbits in the low activity mode all follow the same trajectory, a stable, non-oscillating rest state, and a specific oscillating pattern as active state. Conversely, orbits in the high activity mode alternate between a rest state of small oscillations and an active state of oscillations at a high activity level. Consecutive bursts follow a different trajectory, where all orbits appear to
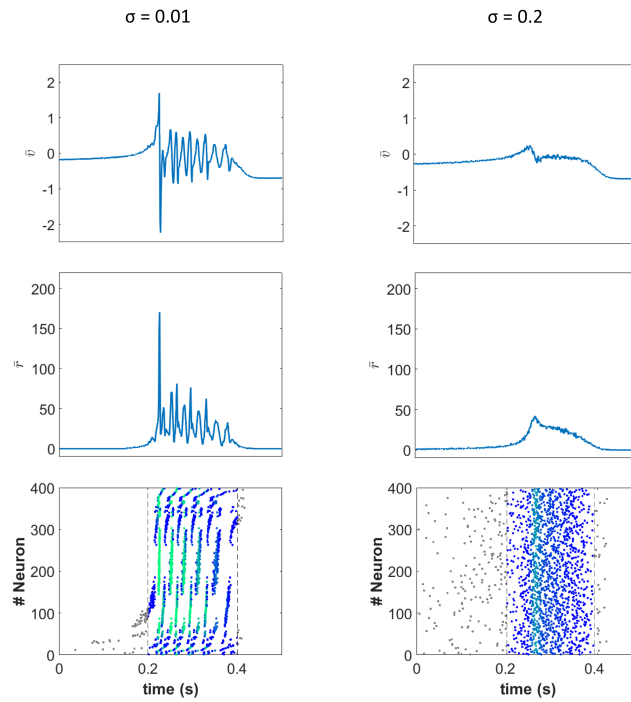
28

Figure 21: Visualisation of the effect of individual noise on the burst shape. The top plots show the $\bar{v}$-evolution of one burst, the middle plots show the $\bar{r}$-evolution of one burst, and at the bottom there are raster plots showing one burst each, displaying 400 selected neurons order by η. On the left, one representative burst with a standard deviation of the noise $\sigma = 0.01$. At the right, one representative burst from a simulation where this standard deviation was increased to $\sigma = 0.2$. Increasing σ has flattened the burst shape.
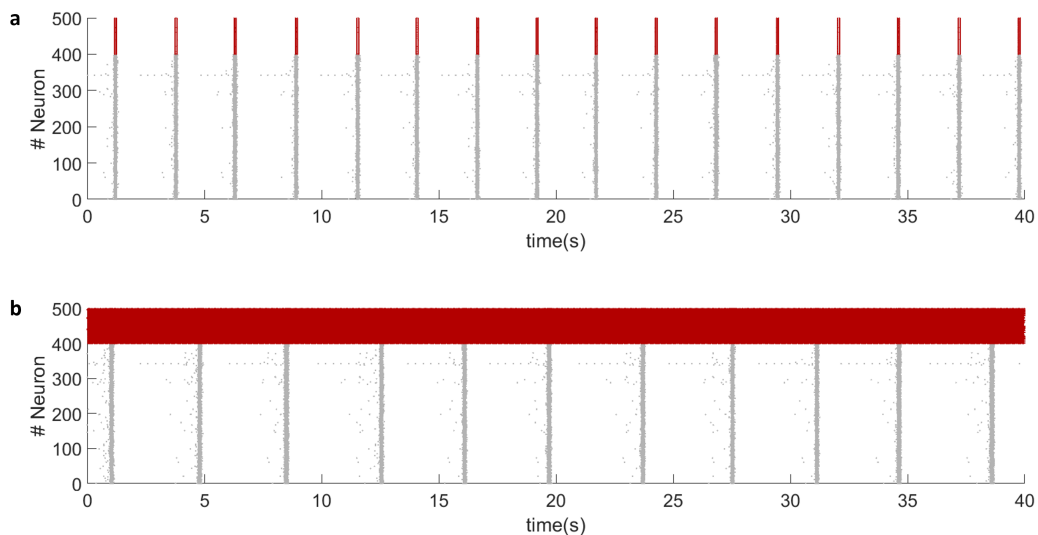
Figure 22: Two full simulations of the two-population model with an excitatory and an inhibitory population. Spikes of excitatory neurons are visualised as grey points, those of inhibitory neurons are shown in red. A simulation for the first mode, with $\eta_{0i} = -0.5$, is shown in **a**. Here, inhibitory neurons are intrinsically inactive. Their activity is synchronised with that of the excitatory neurons, showing the same bursting pattern. A simulation for the second mode with intrinsically active inhibitory neurons, with $\eta_{0i} = 0.5$, is shown in **b**. There is sustained spiking of the inhibitory neurons, the excitatory neurons still form a bursting pattern.

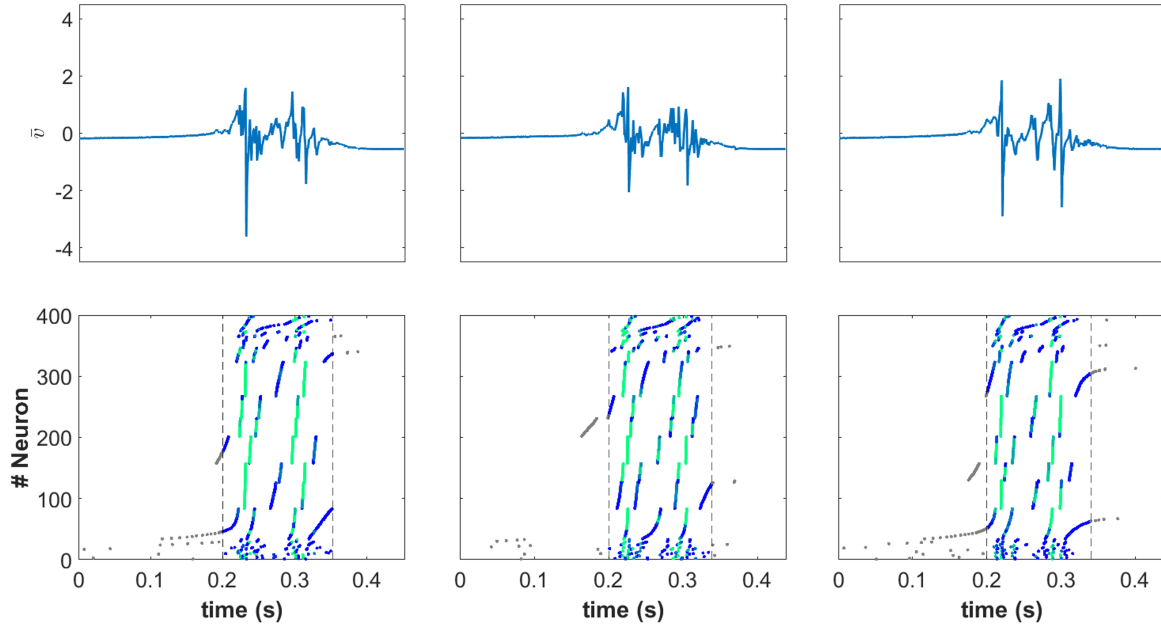**Figure 23:** Three consecutive bursts from a simulation of the two population model in a low activity mode ($\eta_{0i} = -0.5$), with $p_{Syn} = 1$. The top plots show the burst shape in $\bar{v}$-evolution, the bottom raster plots show the spiking activity of 400 selected excitatory neurons, ordered by η. Green points are spikes at a moment of high firing rate.

oscillate around a common limit cycle.

3.5   Simulations and EEG

The bursts in our simulations all share a considerably similar burst onset pattern. All bursts start abruptly with a peak, followed by oscillations with smaller amplitude. Examples of this pattern are the bursts in Figure 17. Comparing this to the bursts in Figure 1, we see that our simulations mostly resemble the burst pattern of BSIB. We do not find the gradual burst onset seen in BSNIB in our simulations. The variation in oscillation amplitude seen in BSNIB, however, also occurs in our simulations with inhibition.
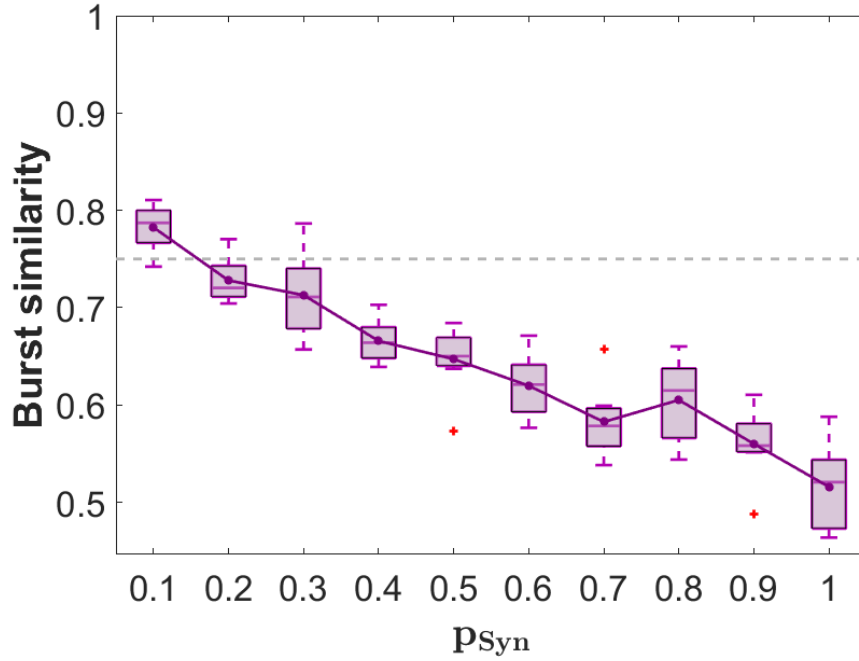
Figure 24: Mean values of burst similarity for simulations of the two-population model with excitation and inhibition, for eight different network realisations and for different synaptic coupling probabilities p_{Syn}. The threshold for identical bursts is considered $q = 0.75$, shown as a dashed grey line. Connected purple points show the mean values of q of the different networks for a given p_{Syn}, the purple boxes show the median and quartiles. Outliers are visualised as red crosses. For $p_{Syn} > 0.1$, the mean values of q are below the threshold for identical bursts.

Figure 25: Three consecutive bursts from a simulation of the two population model in a high activity mode ($\eta_{0i} = 0.5$), with $p_{Syn} = 1$. The top plots show the burst shape in $\bar{v}$-evolution, the bottom raster plots show the spiking activity of 400 selected excitatory neurons, ordered by η. Green points are spikes at a moment of high firing rate.

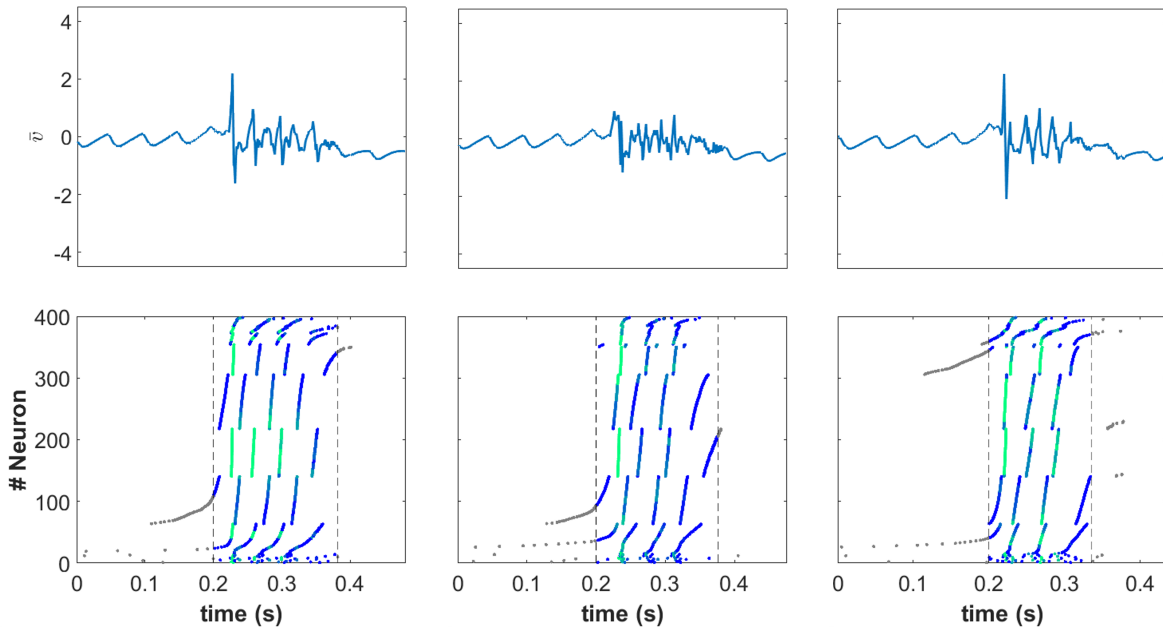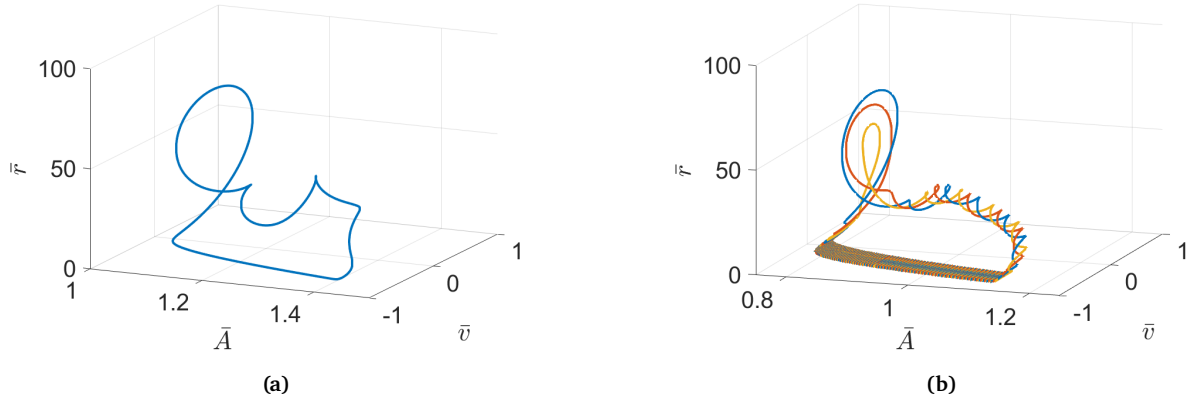**Figure 26:** Simulations of the two-population neural mass model, with one excitatory and one inhibitory population. In (a), the inhibitory population is set in a low activity mode, here $\eta_{0i} = -1$. Only one burst is shown, because all burst follow the same trajectory. In (b), the inhibitory population is set in a high activity mode, here $\eta_{0i} = 1$. Three bursts are shown in different colours, and all show a different evolution. Other parameters are as in Table 2, except $\eta_{0e} = 1$.

Table 2: Parameter values used for simulations of the two-population model: a coupled excitatory and inhibitory population.

Symbol	Value	Unit	Parameter description
τ	10	ms	membrane time constant
α_{ee}	1/2	ms^{-1}	e to e synaptic rise/decay rate
α_{ei}	1/5	ms^{-1}	i to e synaptic rise/decay rate
α_{ie}	1/2	ms^{-1}	e to i synaptic rise/decay rate
α_{ii}	1/5	ms^{-1}	i to i synaptic rise/decay rate
k_e	0	-	gap junction coupling strength for population e
k_i	0	-	gap junction coupling strength for population i
J_{ee}	4	-	e to e synaptic coupling strength
J_{ei}	-1	-	i to e synaptic coupling strength
J_{ie}	4	-	e to i synaptic coupling strength
J_{ii}	-1	-	i to i synaptic coupling strength
Δ_e	0.01	-	external heterogeneous current distribution HWHM for population e
Δ_i	0.01	-	external heterogeneous current distribution HWHM for population i
η_{0e}	0.5	-	external heterogeneous current distribution center for population e
η_{0i}	variable	-	external heterogeneous current distribution center for population i
$I^{(e)}$	0	-	time-varying input current for population e
$I^{(i)}$	0	-	time-varying input current for population i
τ_A	5000	ms	adaptation time constant
a_e	0.5	-	adaptation parameter

4 Discussion

We start by interpreting the results that we obtained. Then, we formulate recommendations for the continuation of this project. We conclude by stating our most prominent findings.

4.1 Interpretation of the results

We identified bursting dynamics in our version of the next-generation neural mass model. Moreover, we evaluated the effect of different parameter settings on the behaviour of the neural mass and microscopic model. The body of our results shows the behaviour of the microscopic model for different synaptic coupling structures, and after implementing an additional inhibitory neuronal population. Here, we discuss these results.

Bursting regimes exist in our next-generation neural mass models
We found a bursting mode of the next-generation neural mass model, and showed that it exists for the same parameter values in the corresponding microscopic model. The active state of the burster is given by a branch of stable focus equilibria. Hereby, the bursts show damped oscillations followed by a non-oscillating high activity (firing rate) state. More naturally, the active state is given by sustained, high-amplitude oscillations, as in most bursters described in [28]. In our microscopic model, the burster shows small, finite-size driven oscillations around the stable focus after initial damped oscillations during the burst. In single neuron models, examples with a sustained oscillatory active states are the Hodgkin-Huxley model with a slow persistent sodium current, or the Morris-Lecar model with a slow calcium current [28]. Not that these single-neuron models can not be directly related to our models of networks of neurons. An example of bursting behaviour with an oscillatory active state on a network scale is the mean-field model in [29]. There, the active state of a burst-suppression pattern is given by oscillations on a stable limit cycle. The bifurcation of the rest state is a Hopf bifurcation, and the bifurcation of the active state is a cyclic fold bifurcation. In our current one-population model, we did not find other bifurcations than a fold bifurcation to escape the rest state.

The mean SFA description quickly deviates from the individual description
For incorporating the slow dynamics of SFA in the mean-field reduction, we needed to assume that the evolution of the neuron-specific adaptation variables A_j can accurately be approximated by the evolution of their population mean $\bar{A}$. We tested this assumption by evaluating the dependence of differences between both descriptions on Δ, which defines the width of the distribution of the neuron-specific background currents η_j. The value of η_j can be interpreted as the intrinsic excitability of neuron j, and we hypothesized that if these are similar enough between neurons, i.e. Δ is sufficiently small, firing patterns of individual neurons are similar enough to justify this assumption on adaptation. Our results show that for $\Delta \leq 0.01$, the differences between individual adaptation and the approximation are acceptable (the relative difference is < 0.05). Therefore we expected that there is a good agreement between the microscopic model and mean-field model when these values of Δ are used. We also found that for larger values of Δ, differences between both descriptions grow fast. Other studies used much larger values of Δ, e.g. $\Delta = 1$ in [16, 27] and $\Delta = 2$ in [26].

Sparse gap junction coupling has negligible effect
We evaluated the effect of gap junction coupling between neurons on the model behaviour by two approaches. First, we varied the gap junction coupling strength κ in the mean-field model, as was also done in previous studies of next generation neural masses [19–21]. Consistent with their

results, we found that the incorporation of gap junction coupling in the model is crucial for the occurrence of Hopf bifurcations in a purely excitatory regime ($J > 0$). Varying κ induces shifting of the Hopf bifurcation branch. When κ was chosen high enough, the branch moved between the two fold bifurcation branches, which is the bistability region where we find our bursting behaviour. Strong coupling with gap junctions induced much higher amplitude oscillations in the active state in the microscopic model, but still dampened towards the end of the burst as we found without gap junctions.

Second, we varied the number of gap junctions per neuron in the microscopic network. This caused a substantial reduction in the amplitude of oscillations, and we showed that the bursting pattern for this sparse coupling resembles the bursting pattern with no gap junctions. Only the equilibrium value of $\bar{v}$ differs between the two scenarios, due to the additional membrane potential coupling provided by the still present gap junctions. This single minor difference justified our decision to remove gap junctions from the model for all remaining simulations.

We expected gap junctions to play an important role in the formation of BS patterns, because of their central role in the emergence of oscillatory states in previous next-generation neural mass models [19–21]. We also identified this role in our neural mass model in Figure 12, but found that the effect was not retained in networks with a realistic number of gap junctions. From a clinical point of view, Hofmeijer et al. [3] proposed a role for gap junctions in BS, since gap junctions are preserved where chemical synapses fail during ischemia. This suggests that gap junctions should not yet be discarded completely.

SFA causes burst shape variation in all-to-all coupled networks
In all-to-all coupled networks, i.e. $p_{Syn} = 1$, we found values of q below the burst similarity threshold. Simulations of these networks show two groups of bursts that are dissimilar. The cause for these distinctive patterns was shown to be the individual SFA, the evolution of A_j deviates considerably from the population mean $\bar{A}$. For implementing SFA into the microscopic and mean-field model, we assumed that the individual A_j can be approximated by $\bar{A}$. Our result shows that this assumption does not hold in our model.

These findings show that a reduction of individual SFA to population SFA is not obviously valid. For larger values of Δ, we expect the individual and population SFA to deviate even more. The statements in [22, 26] that the two descriptions are sufficiently similar do not hold when the behaviour is studied in detail. Our results emphasise the need for checking the assumptions for model reductions, especially when we use approximations of neuron-individual effects.

The individual SFA also affects assumptions at the core of our mean-field reduction. The central assumption of a unimodal distribution of V for similar η fails, because of the individual SFA. The disruption of synchrony of neurons with very similar η_j due to different evolution of A_j causes this distribution to have two modes, at least. For very small values of Δ we might find that the assumptions hold, but only because bringing $\Delta \to 0$ removes the heterogeneity of the neurons. The result would be a network of identical neurons.

We propose an important role for a, the adaptation parameter, in the formation of specific burst shapes. Especially the division into two groups of similar bursts for p_{Syn} shown in Figure 17 is caused by the choice of a. With large a, there is a fast reduction in neuronal firing rate after few spikes, and bursts will be short. Conversely, bursts will be longer with small a. In other words, a determines the burst duration. In turn, the duration of the burst determines what neuron spikes last during that burst, and, as argued before, starts spiking later in the consecutive burst. The disruption of the spiking pattern, as visualised in Figure 18, occurs at this specific neuron. In the simulation in Figure 17, our choice of a resulted in this being a neuron in the middle of the spiking pattern. The duration of the consecutive bursts then caused this to become an alternating pattern. A different choice of a would result in very different burst shapes, and the distribution of cross-correlations between bursts in the simulation would no longer be bimodal.

34

The described effect of individual SFA remains for smaller values of p_{Syn}, but in reduced form. Variations in synaptic input due to random sparse synaptic coupling reduce the distinctive effect of SFA.

Sparse synaptic coupling induces more similar bursts

When we reduced the synaptic coupling probability, bursts became more similar in all considered model realisations. This opposes our hypothesis: we expected to find more irregular behaviour after reducing the number of synaptic connections. Firstly, all neurons remain synchronised in the formation of bursts: during bursts, all neurons spike in the sparsely coupled networks. Also, moments of high within-burst synchrony remain, reflected by peaks in the burst shape. At large p_{Syn}, smaller groups of neurons synchronise during a burst, causing more small and irregular peaks in the burst shape. Reducing p_{Syn} results in larger synchronised groups, but with more dispersed activity. In the burst shape, this is reflected by a smoother signal with lower amplitude peaks.

Our hypothesis of more clustered activity at smaller p_{Syn} was disproved for these models by our results. The hypothesis might hold in a model with different settings. A different slow mechanism than SFA could make a large difference, also allowing the choice for a larger value of Δ, which would bring more intrinsic heterogeneity into the model. Alternatively, a further reduction of p_{Syn} might result in the hypothesised behaviour, but caution is needed to not arrive at physiologically unrealistic values.

Individual noise flattens the burst shape

Adding an independent noise term to each neuron causes the burst shape to flatten, large amplitude peaks reflecting a high level of synchrony disappear. Before, we found that without taking the effect of A_j into account, there is synchronisation of neurons with similar η_j, which are neurons with similar intrinsic excitability and thus a similar firing rate when they receive sufficient input. Noise induces random shifts in the phase of individual neurons, possibly desynchronising the phase-evolution of neurons although their η_j is similar. The strength of the desynchronising effect depends on the neuron's phase when it receives a large noisy input, through the bell-shaped phase-response-curve of a QIF-neuron.

Two modes of inhibition show different burst patterns

When extending our model with an inhibitory population, we chose to consider two modes: one where the inhibitory population has a high level of intrinsic activity, reflected by $\eta_{0i} > 0$, and one where this population has a low level of intrinsic activity, $\eta_{0i} < 0$. Simulations of the two-population model in low activity mode show more variation in oscillation amplitude than observed in our purely excitatory model. A clear influence of SFA on the burst shape remains clear from the raster plots in Figure 23.

In high activity mode, sustained inhibitory activity causes the rest state of the bursting behaviour to become oscillatory. Figure 25 also shows a little variation in burst onset pattern for the second burst. Arguably, the rest state oscillations can be the cause of more different burst onset patterns. At the start of a burst, the network state could be at any position on the rest state oscillation, causing the network to be in a different state at burst onset during different bursts. This opposes the bursts initiating from the stable fixed point as in e.g. the low activity mode discussed in the preceding paragraph, where the network state at burst onset is approximately equal for every burst.

The dynamics of the two-population neural mass model in the high activity mode, shown in Figure 26b, are remarkable. There is not a clear, single attractor as for the low activity mode in Figure 26a. Orbits from different bursts show different patterns, but seem to oscillate around a common unstable limit cycle. This kind of behaviour could be indicative of an attracting limit cycle as in the low activity state having undergone a Neimark-Sacker bifurcation. Liley et al.

[29] found such a torus bifurcation in the fast subsystem of their mean-field model. In our case, this bifurcation would have occurred in the complete system.

Simulations show a tentative resemblance with only BSIB EEG

We related our results to the clinical motivation for this project: different patterns of burst-suppression on the EEG. We compared the model simulations to the EEGs with BSNIB and BSIB from Figure 1.

In BSNIB we see a gradual increase in activity, whereas in BSIB the burst starts with a high-amplitude peak. We found that the onset in our simulations is most similar to the bursts seen in BSIB. The pattern of burst onset is determined by the type of bifurcation of the rest state. In our burster, this is a fold bifurcation: the solution jumps from the stable rest state to the stable active state. This jump causes the large peak at burst onset. Izhikevich [28] also describes bursters where the bifurcation of the rest state is a bifurcation of a limit cycle, where a more gradual burst onset is possible. To find BSNIB, we might need a different bifurcation of the rest state in a burster.

Our simulated bursts show oscillations that dampen towards burst termination. This is similar to the burst progression seen in Figure 1 for BSIB. In BSNIB, oscillations vary in amplitude during the burst. We found such behaviour in our two-population model, but these simulations are far from similar to BSNIB patterns on the EEG.

Spatial properties are not reflected in our models, because we only considered local neural masses representing local cortical populations of neurons. To gain insight into the spatial synchrony involved in BS, more elaborate models of coupled neural masses are needed, possibly incorporating also subcortical populations. Neural field models are an alternative option, which have previously been studied in the context of next-generation neural mass models [21, 41].

4.2   Recommendations

Building on our results, we have suggestions for further research on the emergence of non-identical bursts. First, and most important, we found that the assumptions needed for the implementation of SFA in the next-generation neural mass model do not hold in the parameter regimes that we investigated. We expect the assumptions to fail also in other parameter regimes, since the effect we observed seems independent of parameter settings. A possible replacement for SFA as a slow modulatory mechanism is short-term synaptic depression (SD). The validity of a reduction to a next-generation neural mass model in the presence of SD has been thoroughly studied [23–25], although none discuss the behaviour of the microscopic model to the same level of detail as we do here. An advantage of SD is that through this mechanism, a spike of one neuron affects the SD-variable of all neurons it has an efferent synaptic connection with. This contrasts the mechanism of SFA, where a spike of one neuron affects its own SFA-variable. Hereby, SD is not a neuron-specific effect, and assumptions for a mean-field reduction are more easily satisfied. Gast et al. [26] show that bursting is possible in a next-generation neural mass model with SD. Taher et al [25] also show bursting in a next-generation neural mass model with SD, only they do not consider SD as the slow modulatory mechanism but rather a slowly varying applied current.

Our restrictions on the choice of Δ are caused by a growing difference between individual and population SFA for increasing Δ. When replacing SFA by a different slow mechanism, we are less restricted in our choice of Δ. Values between 0.5 and 2 are used in other studies [16, 26, 27], and this increased heterogeneity of neurons will induce different model dynamics. We already showed how the bifurcation structure of the one-population neural mass model in J and η_0 depends on Δ in Figure 15, but did not yet investigate how the behaviour of the microscopic model depends on the choice of Δ.

A second recommendation concerns the effect of inhibition. In Section 1.1, we shortly discuss

the critical role of inhibition in burst-suppression. Our results on the effect of complementing the excitatory neural mass with an inhibitory population allow several natural extensions. Firstly, a thorough bifurcation analysis of the two-population model will give insight into the bursting behaviour we observed in our simulations. Exploration of the parameter space spanned by the synaptic coupling strengths $J_{(..)}$ and neuron-heterogeneity parameters $\eta_{0(\cdot)}$ and $\Delta_{(\cdot)}$ would be a first step, possibly revealing new bursting regimes. Secondly, adjusting the inhibitory post-synaptic response will allow modelling the effect of propofol, which is known to heavily increase the decay time constant of the inhibitory post-synaptic potential [29]. Describing the inhibitory synaptic response as a dual exponential with two separate time constants allows incorporating this effect, as opposed to the α-synapse we implemented in our model, with an equal rise and decay time constant. In a different model setup and applying this anesthetic effect, inhibition could act as the slow mechanism in a bursting regime.

Furthermore, the effect of noise needs further studying. In our models, we only implemented individual noise, i.e. we applied an independent Gaussian noise term to each neuron. This noise with mean 0 has no effect on the neural mass model. However, in a realistic setting, neuronal cortical populations also receive common noisy input, e.g. interpreted as random subcortical input. This type of noise would also affect the neural mass model, and could be an important factor in finding more unpredictable behaviour of the model. In the microscopic model, this noise term would not be independent between neurons, but a common noise term that is random in time.

Finally, when more qualitatively comparing simulations to EEG, the models need finetuning of specific burst features such as the inter-burst-interval and burst duration. Given specific parameter settings of the fast subsystem, these two timescale features are determined by the parameters that define the slow mechanism. In our models, with SFA, these parameters are the adaptation time constant τ_A and the adaptation strength a. When implementing a different slow mechanism, also the strength of the modulatory effect and its decay time constant would contribute most to these burst features.

4.3 Conclusion

In our one- and two-population neural mass models, we identified bursting dynamics where the active state is given by damped oscillations. In our microscopic models, we found that spike-frequency adaptation, the slow mechanism that accounts for the alternation between rest and active state, plays a crucial role in the formation of burst patterns, and that its neuron-individual behaviour causes a central assumption in the exact mean-field reduction to fail. This greatly influences the burst shapes in simulations and restricts analysis of other model adjustments affecting burst shape. Beside the need for an alternative slow modulatory mechanism, the bursting dynamics in our microscopic two-population model indicate that further exploration of the two-population mean-field model and the implementation of population noise are promising future directions for research on the emergence of BSNIB in neuronal network models.

References

[1] E. Niedermeyer, D. L. Sherman, R. J. Geocadin, H. C. Hansen, and D. F. Hanley. "The Burst-Suppression Electroencephalogram", *Clinical Electroencephalography* 30.3 (1999), pp. 99–105. DOI: 10.1177/155005949903000305.

[2] A. Shanker, J. H. Abel, G. Schamberg, and E. N. Brown. "Etiology of Burst Suppression EEG Patterns", *Frontiers in Psychology* 12 (2021). DOI: 10.3389/fpsyg.2021.673529.

[3] J. Hofmeijer, M. C. Tjepkema-Cloostermans, and M. J. A. M. van Putten. "Burst-suppression with identical bursts: A distinct EEG pattern with poor outcome in postanoxic coma", *Clinical Neurophysiology* 125.5 (2014), pp. 947–954. DOI: 10.1016/j.clinph.2013.10.017.

[4] M. Brandon Westover, S. Ching, V. M. Kumaraswamy, O. Akeju, E. Pierce, S. S. Cash, R. Kilbride, E. N. Brown, and P. L. Purdon. "The human burst suppression electroencephalogram of deep hypothermia", *Clinical Neurophysiology* 126.10 (2015), pp. 1901–1914. DOI: 10.1016/j.clinph.2014.12.022.

[5] B. J. Ruijter, J. Hofmeijer, H. G. E. Meijer, and M. van Putten. "Synaptic damage underlies EEG abnormalities in postanoxic encephalopathy: A computational study", *Clinical Neurophysiology* 128.9 (2017), pp. 1682–1695. DOI: 10.1016/j.clinph.2017.06.245.

[6] D. Kroeger and F. Amzica. "Hypersensitivity of the Anesthesia-Induced Comatose Brain", *The Journal of Neuroscience* 27.39 (2007), p. 10597. DOI: 10.1523/JNEUROSCI.3440-07.2007.

[7] J.-F. Ferron, D. Kroeger, O. Chever, and F. Amzica. "Cortical Inhibition during Burst Suppression Induced with Isoflurane Anesthesia", *The Journal of Neuroscience* 29.31 (2009), p. 9850. DOI: 10.1523/JNEUROSCI.5176-08.2009.

[8] F. Amzica. "What does burst suppression really mean?", *Epilepsy & Behavior* 49 (2015), pp. 234–237. DOI: https://doi.org/10.1016/j.yebeh.2015.06.012.

[9] A. L. Hodgkin and A. F. Huxley. "A quantitative description of membrane current and its application to conduction and excitation in nerve", *The Journal of Physiology* 117.4 (1952), pp. 500–544. DOI: 10.1113/jphysiol.1952.sp004764.

[10] H. R. Wilson and J. D. Cowan. "Excitatory and Inhibitory Interactions in Localized Populations of Model Neurons", *Biophysical Journal* 12.1 (1972), pp. 1–24. DOI: 10.1016/S0006-3495(72)86068-5.

[11] A. Pathak, D. Roy, and A. Banerjee. "Whole-Brain Network Models: From Physics to Bedside", *Frontiers in Computational Neuroscience* 16 (2022). DOI: 10.3389/fncom.2022.866517.

[12] M. Breakspear. "Dynamic models of large-scale brain activity", *Nature Neuroscience* 20.3 (2017), pp. 340–352. DOI: 10.1038/nn.4497.

[13] G. Deco, V. K. Jirsa, P. A. Robinson, M. Breakspear, and K. Friston. "The Dynamic Brain: From Spiking Neurons to Neural Masses and Cortical Fields", *PLOS Computational Biology* 4.8 (2008), e1000092–. DOI: 10.1371/journal.pcbi.1000092.

[14] S. Coombes. "Large-scale neural dynamics: Simple and complex", *NeuroImage* 52.3 (2010), pp. 731–739. DOI: 10.1016/j.neuroimage.2010.01.045.

[15]   D. T. J. Liley, B. L. Foster, and I. Bojak. "Co-operative Populations of Neurons: Mean Field Models of Mesoscopic Brain Activity", *Computational Systems Neurobiology*. Dordrecht: Springer Netherlands, 2012, pp. 317–364. DOI: 10.1007/978-94-007-3858-4{_}11.

[16]   E. Montbrió, D. Pazó, and A. Roxin. "Macroscopic description for networks of spiking neurons", *Physical Review X* 5.2 (2015). DOI: 10.1103/PhysRevX.5.021028.

[17]   E. Ott and T. M. Antonsen. "Low dimensional behavior of large systems of globally coupled oscillators", *Chaos: An Interdisciplinary Journal of Nonlinear Science* 18.3 (2008), p. 037113. DOI: 10.1063/1.2930766.

[18]   Á. Byrne, M. J. Brookes, and S. Coombes. "A mean field model for movement induced changes in the beta rhythm", *Journal of Computational Neuroscience* 43.2 (2017), pp. 143–158. DOI: 10.1007/s10827-017-0655-7.

[19]   B. Pietras, F. Devalle, A. Roxin, A. Daffertshofer, and E. Montbrió. "Exact firing rate model reveals the differential effects of chemical versus electrical synapses in spiking networks", *Physical Review E* 100.4 (2019), p. 42412. DOI: 10.1103/PhysRevE.100.042412.

[20]   E. Montbrió and D. Pazó. "Exact Mean-Field Theory Explains the Dual Role of Electrical Synapses in Collective Synchronization", *Physical Review Letters* 125.24 (2020), p. 248101. DOI: 10.1103/PhysRevLett.125.248101.

[21]   Á. Byrne, J. Ross, R. Nicks, and S. Coombes. "Mean-Field Models for EEG/MEG: From Oscillations to Waves", *Brain Topography* 35.1 (2022), pp. 36–53. DOI: 10.1007/s10548-021-00842-4.

[22]   A. Ferrara, D. Angulo-Garcia, A. Torcini, and S. Olmi. "Population spiking and bursting in next-generation neural masses with spike-frequency adaptation", *Physical Review E* 107.2 (2023), p. 24311. DOI: 10.1103/PhysRevE.107.024311.

[23]   H. Taher, A. Torcini, and S. Olmi. "Exact neural mass model for synaptic-based working memory", *PLOS Computational Biology* 16.12 (2020), e1008533–. DOI: 10.1371/journal.pcbi.1008533.

[24]   R. Gast, T. R. Knösche, and H. Schmidt. "Mean-field approximations of networks of spiking neurons with short-term synaptic plasticity", *Physical Review E* 104.4 (2021). DOI: 10.1103/PhysRevE.104.044310.

[25]   H. Taher, D. Avitabile, and M. Desroches. "Bursting in a next generation neural mass model with synaptic dynamics: a slow–fast approach", *Nonlinear Dynamics* 108.4 (2022), pp. 4261–4285. DOI: 10.1007/s11071-022-07406-6.

[26]   R. Gast, H. Schmidt, and T. R. Knösche. "A Mean-Field Description of Bursting Dynamics in Spiking Neural Networks with Short-Term Adaptation", *Neural Computation* 32.9 (2020), pp. 1615–1634. DOI: 10.1162/neco{_}a{_}01300.

[27]   D. Avitabile, M. Desroches, and G. B. Ermentrout. "Cross-scale excitability in networks of quadratic integrate-and-fire neurons", *PLOS Computational Biology* 18.10 (2022), e1010569–. DOI: 10.1371/journal.pcbi.1010569.

[28]   E. M. Izhikevich. "Neural Excitability, Spiking and Bursting", *International Journal of Bifurcation and Chaos* 10.06 (2000), pp. 1171–1266. DOI: 10.1142/S0218127400000840.

[29]   D. T. Liley and M. Walsh. "The mesoscopic modelling of burst suppression during anaesthesia", *Frontiers in Computational Neuroscience* APR 2013 (2013). DOI: 10.3389/fncom.2013.00046.

[30]   A. D. Rae-Grant and Y. W. Kim. "Type III intermittency: a nonlinear dynamic model of EEG burst suppression", *Electroencephalography and Clinical Neurophysiology* 90.1 (1994), pp. 17–23. DOI: 10.1016/0013-4694(94)90109-0.

[31] S. Ching, P. L. Purdon, S. Vijayan, N. J. Kopell, and E. N. Brown. "A neurophysiological–metabolic model for burst suppression", *Proceedings of the National Academy of Sciences* 109.8 (2012), pp. 3095–3100. DOI: 10.1073/pnas.1121461109.

[32] T. Schwalger, M. Deger, and W. Gerstner. "Towards a theory of cortical columns: From spiking neurons to interacting neural populations of finite size", *PLOS Computational Biology* 13.4 (2017), e1005507–. DOI: 10.1371/journal.pcbi.1005507.

[33] V. Schmutz, W. Gerstner, and T. Schwalger. "Mesoscopic population equations for spiking neural networks with synaptic short-term plasticity", *The Journal of Mathematical Neuroscience* 10.1 (2020), p. 5. DOI: 10.1186/s13408-020-00082-z.

[34] M. Gerster, H. Taher, A. Škoch, J. Hlinka, M. Guye, F. Bartolomei, V. Jirsa, A. Zakharova, and S. Olmi. "Patient-Specific Network Connectivity Combined With a Next Generation Neural Mass Model to Test Clinical Hypothesis of Seizure Propagation", *Frontiers in Systems Neuroscience* 15 (2021). DOI: 10.3389/fnsys.2021.675272.

[35] B. Pietras, V. Schmutz, and T. Schwalger. "Mesoscopic description of hippocampal replay and metastability in spiking neural networks with short-term plasticity", *PLOS Computational Biology* 18.12 (2022), pp. 1–46. DOI: 10.1371/journal.pcbi.1010809.

[36] R. D. Traub, M. A. Whittington, E. H. Buhl, F. E. N. LeBeau, A. Bibbig, S. Boyd, H. Cross, and T. Baldeweg. "A Possible Role for Gap Junctions in Generation of Very Fast EEG Oscillations Preceding the Onset of, and Perhaps Initiating, Seizures", *Epilepsia* 42.s2 (2001), pp. 153–170. DOI: 10.1046/j.1528-1157.2001.4220153.x.

[37] R. D. Traub, R. Duncan, A. J. C. Russell, T. Baldeweg, Y. Tu, M. O. Cunningham, and M. A. Whittington. "Spatiotemporal patterns of electrocorticographic very fast oscillations (>80 Hz) consistent with a network model based on electrical coupling between principal neurons", *Epilepsia* 51.8 (2010), pp. 1587–1597. DOI: 10.1111/j.1528-1167.2009.02420.x.

[38] C. Börgers and N. Kopell. "Effects of Noisy Drive on Rhythms in Networks of Excitatory and Inhibitory Neurons", *Neural Computation* 17.3 (2005), pp. 557–608. DOI: 10.1162/0899766053019908.

[39] A. Dhooge, W. Govaerts, Y. A. Kuznetsov, H. G. E. Meijer, and B. Sautois. "New features of the software MatCont for bifurcation analysis of dynamical systems", *Mathematical and Computer Modelling of Dynamical Systems* 14.2 (2008), pp. 147–175. DOI: 10.1080/13873950701742754.

[40] M. Stimberg, R. Brette, and D. F. M. Goodman. "Brian 2, an intuitive and efficient neural simulator", *eLife* 8 (2019), e47314. DOI: 10.7554/eLife.47314.

[41] Á. Byrne, R. D. O'Dea, M. Forrester, J. Ross, and S. Coombes. "Next-generation neural mass and field modeling", *Journal of Neurophysiology* 123.2 (2019), pp. 726–742. DOI: 10.1152/jn.00406.2019.

A Appendix

A.1 Model equations

The microscopic model is given by:

$$\tau \dot{V}_j = V_j^2 + \eta_j + Js_j\tau + \kappa g_j + I - A_j, \tag{A.1}$$

$$Qs_j(t) = \frac{1}{|S_j|} \sum_{n \in S_j} \sum_{k, t_n^k < t} \delta(t - t_n^k), \tag{A.2}$$

$$\tau_A \dot{A}_j = -A_j + a \sum_{k, t_j^k < t} \delta(t - t_j^k), \tag{A.3}$$

with reset rule for V_j: if $V_j > V_{thr}$, $V_j \leftarrow V_{reset}$, synaptic dynamics given by $Q = (1 + \frac{1}{\alpha}\frac{d}{dt})^2$ for the α-synapse, and the gap junction current g_j:

$$g_j(t) = \frac{1}{N} \sum_{m \in G_j} (V_m(t) - V_j(t)).$$

The corresponding mean-field model is given by:

$$
\begin{aligned}
\tau \dot{r} &= -\kappa r + \frac{\Delta}{\pi \tau} + 2rv, \\
\tau \dot{v} &= v^2 + \eta_0 + Js\tau + I - A - (\pi \tau r)^2, \\
Qs &= r, \\
\tau_A \dot{A} &= -A + ar,
\end{aligned}
\tag{A.4}
$$

A.2 Transformation to θ-oscillators

The V-system allows a transformation to an ensemble of coupled oscillators. In the QIF-network described by (2.1), we transform the V-variable to a phase variable θ using the transformation $V_j = \tan\left(\frac{\theta_j}{2}\right)$. Hereby the reset conditions are no longer infinite. The transformation yields a new first-order ODE:

$$\tau \dot{\theta}_j = 1 - \cos\theta_j - \kappa \sin\theta_j + (1 + \cos\theta_j)\left(\eta_j + Js_j\tau + I + \frac{\kappa}{N}\sum_{m \in G_j}\frac{\sin\theta_m}{1 + \cos\theta_m}\right), \tag{A.5}$$

$$\text{if } \theta_j > \theta_{thr}, \theta_j \leftarrow \theta_{reset},$$

where, as $V_{thr} = -V_{reset} \to \infty$, we have $\theta_{thr} = -\theta_{reset} = \pi$. From now we again assume all-to-all coupling, through both the synapses and the gap junctions. The final term of the θ-evolution then reduces to the product of connection strength κ, the mean membrane potential v, and $1 + \cos\theta_j$.

Next, we rewrite the evolution equation in terms of $e^{\pm i\theta}$ to obtain:

$$\tau \dot{\theta} = fe^{i\theta} + \tilde{f}e^{-i\theta} + h, \tag{A.6}$$

where $f = \frac{1}{2}(\eta + Js\tau + I + \kappa v - 1 + i\kappa)$, $\tilde{f} = \frac{1}{2}(\eta + Js\tau + I + \kappa v - 1 - i\kappa)$ and $h = \eta + Js\tau + I + \kappa v + 1$.

In the limit $N \to \infty$ and assuming all-to-all coupling, we describe the phases of all neurons by a continuous probability density function $\rho(\theta|\eta, t)$. The continuity equation described above holds still:

$$\partial_t \rho = -\partial_\theta \rho \dot{\theta}. \tag{A.7}$$

Now, following the approach of Ott and Antonsen [17], we define

$$\int_0^{2\pi} \rho(\theta|\eta, t)\, d\theta = g(\eta),$$

where $g(\eta)$ denotes the continuous distribution of η_j's. The expansion of ρ in a Fourier series in θ is given by:

$$\rho(\theta|\eta, t) = \frac{g(\eta)}{2\pi} \left(1 + \left[\sum_{n=1}^{\infty} f_n(\eta, t)e^{in\theta} + c.c.\right]\right), \tag{A.8}$$

where $c.c.$ denotes the complex conjugate of the term that precedes it. Given this expansion, we consider a restricted class of ρ's where we assume $f_n(\eta, t) = \alpha(\eta, t)^n$ with $|\alpha(\eta, t)| \leq 1$ to avoid divergence.

It is now convenient to define the Kuramoto order parameter for our phase variable θ_j:

$$Z(t) = \frac{1}{N} \sum_{j=1}^{N} e^{i\theta_j},$$

which, for $N \to \infty$, is equal to

$$Z(t) = \int_0^{2\pi} d\theta \int_{-\infty}^{\infty} d\eta \rho(\theta|\eta, t)e^{i\theta}.$$

By use of the following orthogonality property:

$$\int_0^{2\pi} e^{im\theta}e^{in\theta}\, d\theta = \begin{cases} 2\pi, & \text{if } m+n=0 \\ 0, & \text{otherwise} \end{cases}$$

and given our restricted class of ρ's, we write $Z(t)$ as

$$Z(t) = \int_{-\infty}^{\infty} \overline{\alpha(\eta, t)}g(\eta)\, d\eta,$$

and conjugated:

$$\bar{Z}(t) = \int_{-\infty}^{\infty} \alpha(\eta, t)g(\eta)\, d\eta.$$

By using contour integration and applying the residue theorem, we obtain the following result:

$$\bar{Z}(t) = \alpha(\eta_0 - i\Delta, t). \tag{A.9}$$

To find an expression for $\alpha(\eta, t)$, we substitute Eqs. (A.6) and (A.8) into continuity equation (A.7). Expanding the left-hand-side yields

$$\frac{\partial}{\partial t}\rho = \frac{g(\eta)}{2\pi} \left(\sum_{n=1}^{\infty} e^{in\theta} n\alpha(\eta, t)^{n-1}\frac{\partial}{\partial t}\alpha(\eta, t) + \sum_{n=1}^{\infty} e^{-in\theta} n\overline{\alpha(\eta, t)}^{n-1}\frac{\partial}{\partial t}\overline{\alpha(\eta, t)}\right),$$

and the right-hand-side:

$$-\frac{\partial}{\partial \theta}\rho\dot{\theta} = -\frac{g(\eta)}{2\pi\tau}\left(ife^{i\theta} - i\tilde{f}e^{-i\theta}\right)\left(1 + \sum_{n=1}^{\infty} \alpha(\eta, t)^n e^{in\theta} + \overline{\alpha(\eta, t)}^n e^{-in\theta}\right)$$

$$-\frac{g(\eta)}{2\pi\tau}\left(fe^{i\theta} + \tilde{f}e^{-i\theta} + h\right)\left(\sum_{n=1}^{\infty} in\alpha(\eta, t)^n e^{in\theta} - in\overline{\alpha(\eta, t)}^n e^{-in\theta}\right).$$

Equating these partial derivatives and balancing terms in $e^{i\theta}$ yields

$$\tau\frac{\partial}{\partial t}\alpha = -if - i\tilde{f}\alpha^2 - ih\alpha. \tag{A.10}$$

By (A.9), substituting $\eta = \eta_0 - i\Delta$ into (A.10) yields an evolution equation for $\bar{Z}$:

$$\tau\frac{d}{dt}\bar{Z} = -\frac{i}{2}(\eta_0 - i\Delta + Js\tau + I + \kappa v - 1 + i\kappa) - \frac{i}{2}(\eta_0 - i\Delta + Js\tau + I + \kappa v - 1 - i\kappa)\bar{Z}^2$$
$$- i(\eta_0 - i\Delta + Js\tau + I + \kappa v + 1)\bar{Z}.$$

Taking the conjugate of both sides now yields:

$$\tau\frac{d}{dt}Z = \frac{i}{2}(\eta_0 + i\Delta + Js\tau + I + \kappa v - 1 - i\kappa) + \frac{i}{2}(\eta_0 + i\Delta + Js\tau + I + \kappa v - 1 + i\kappa)Z^2$$
$$+ i(\eta_0 + i\Delta + Js\tau + I + \kappa v + 1)Z,$$

which we rewrite to:

$$\tau\frac{d}{dt}Z = \frac{i}{2}(Z+1)^2(\eta_0 + Js\tau + I + \kappa v) - \frac{1}{2}(Z+1)^2\Delta - \frac{i}{2}(Z-1)^2 - \frac{1}{2}(Z^2 - 1)\kappa. \tag{A.11}$$

To arrive at a closed system, we need an expression for s. Under the assumption of all-to-all coupling, s is a global variable, and linear operator Q and firing rate r together describe its evolution:

$$Qs(t) = r(t) = \frac{1}{N}\sum_{j=1}^{N}\sum_{k\in\mathbb{Z}}\delta(t - t_j^k). \tag{A.12}$$

Noting that t_j^k for all k are the roots of $\theta_j(t) - \pi$, and using the exponential representation of the Dirac delta function, we have:

$$\sum_{k\in\mathbb{Z}}\delta(t - t_j^k) = \frac{2}{\tau}\delta(\theta_j - \pi) = \frac{1}{\pi\tau}\sum_{m\in\mathbb{Z}}e^{im(\theta_j - \pi)}. \tag{A.13}$$

Also, the following limit holds:

$$\lim_{N\to\infty}\frac{1}{N}\sum_{j=1}^{N}\delta(t - t_j^k) = \int_0^{2\pi}d\theta\int_{-\infty}^{\infty}d\eta\,\rho(\theta|\eta, t)\,\delta(t - t_j^k). \tag{A.14}$$

Combining (A.13) and (A.14), and substituting (A.8), we rewrite (A.12) to:

$$Qs = \frac{1}{\pi}\sum_{m\in\mathbb{Z}}\int_0^{2\pi}d\theta\int_{-\infty}^{\infty}d\eta\,\frac{g(\eta)e^{im(\theta-\pi)}}{2\pi\tau}\left(1 + \left[\sum_{n=1}^{\infty}\alpha(\eta, t)^n e^{in\theta} + c.c.\right]\right). \tag{A.15}$$

For this case we have the following orthogonality property:

$$\int_0^{2\pi}e^{im(\theta-\pi)}e^{in\theta}\,d\theta = \begin{cases} 2\pi, & \text{if } m + n = 0, m \text{ is even}, \\ -2\pi, & \text{if } m + n = 0, m \text{ is odd}, \\ 0, & \text{otherwise}, \end{cases}$$

which, applied to (A.15), yields:

$$Qs = \frac{1}{\pi\tau}\int_{-\infty}^{\infty}d\eta\,g(\eta)\left(1 + \left[\sum_{m=1}^{\infty}(-1)^m\alpha(\eta, t)^m + c.c.\right]\right).$$

Expanding the brackets and taking the sum out of the integral, we are left with

$$Qs = \frac{1}{\pi\tau} \int_{-\infty}^{\infty} g(\eta)\, d\eta + \frac{1}{\pi\tau} \sum_{m=1}^{\infty} \int_{-\infty}^{\infty} (-1)^m g(\eta)\alpha(\eta,t)^m + (-1)^m g(\eta)\overline{\alpha(\eta,t)}^m \, d\eta.$$

Because $g(\eta)$ is a normalised probability density function, the first integral equals 1. The second integral is evaluated by using contour integration and applying the residue theorem. We combine this to:

$$Qs = \frac{1}{\pi\tau} \left(1 + \sum_{m=1}^{\infty} (-1)^m Z^m + (-1)^m \bar{Z}^m \right).$$

Finally, we rewrite these geometric series using $\sum_{m=1}^{\infty} (-Z)^m = \frac{1}{1+Z} - 1$ for Z and its conjugate, after which we obtain an evolution equation for s in terms of the order parameter Z:
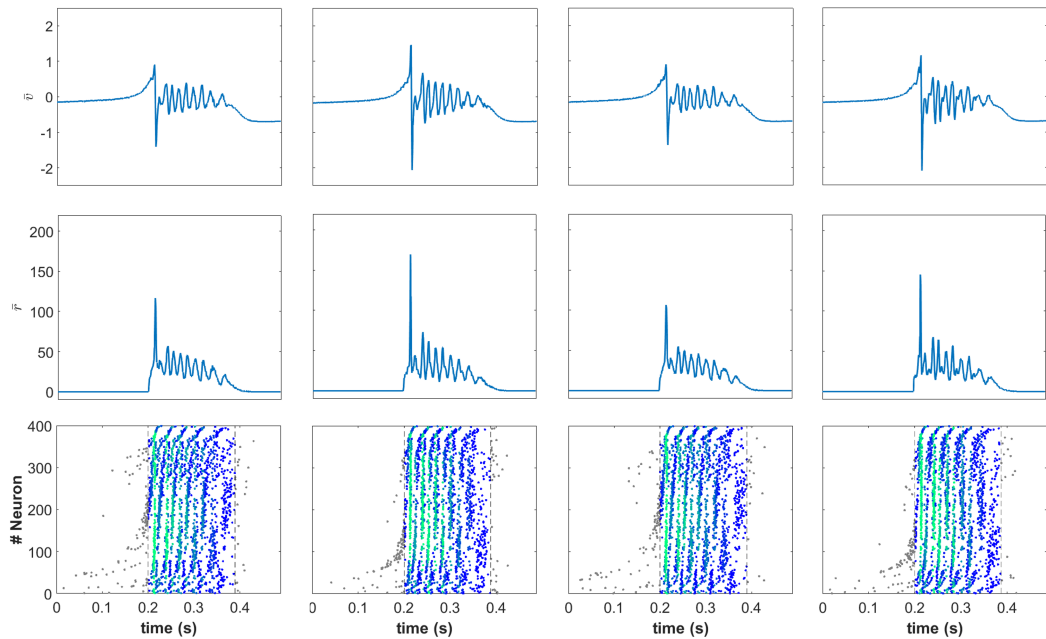
$$Qs = \frac{1}{\pi\tau} \frac{1 - |Z|^2}{1 + Z + \bar{Z} + |Z|^2}. \tag{A.16}$$

This expression for s-evolution and (A.11) form a closed mean-field model.
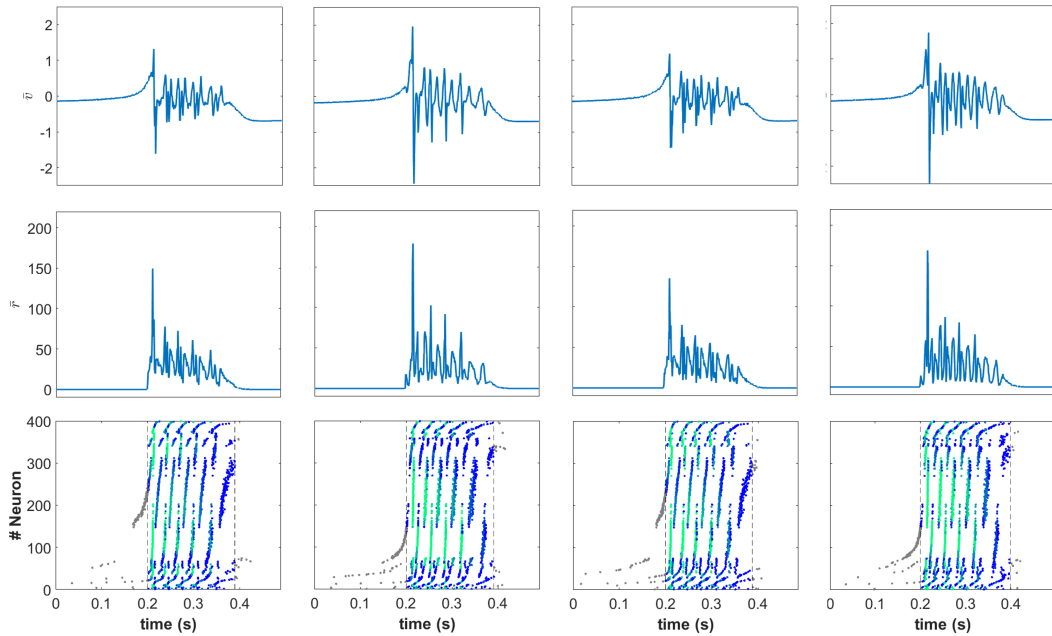
(a)

(b)

Figure 1: Four bursts from a simulation with (a) $p_{Syn} = 0.6$ and (b) $p_{Syn} = 0.1$. Each column shows one burst, with an additional 0.2s before burst onset, and an additional 0.1s after burst termination. The top plots show the evolution of $\bar{v}$, the mean membrane potential of the network, and the middle plots show the evolution of $\bar{r}$, the mean firing rate of the network. The bottom figures show raster plots of the spikes of 400 selected neurons, ordered by η. Neurons with higher η have lower index. Colouring in the raster plots is based on the mean population firing rate at that moment in time. Green points are spikes at a moment of high firing rate.
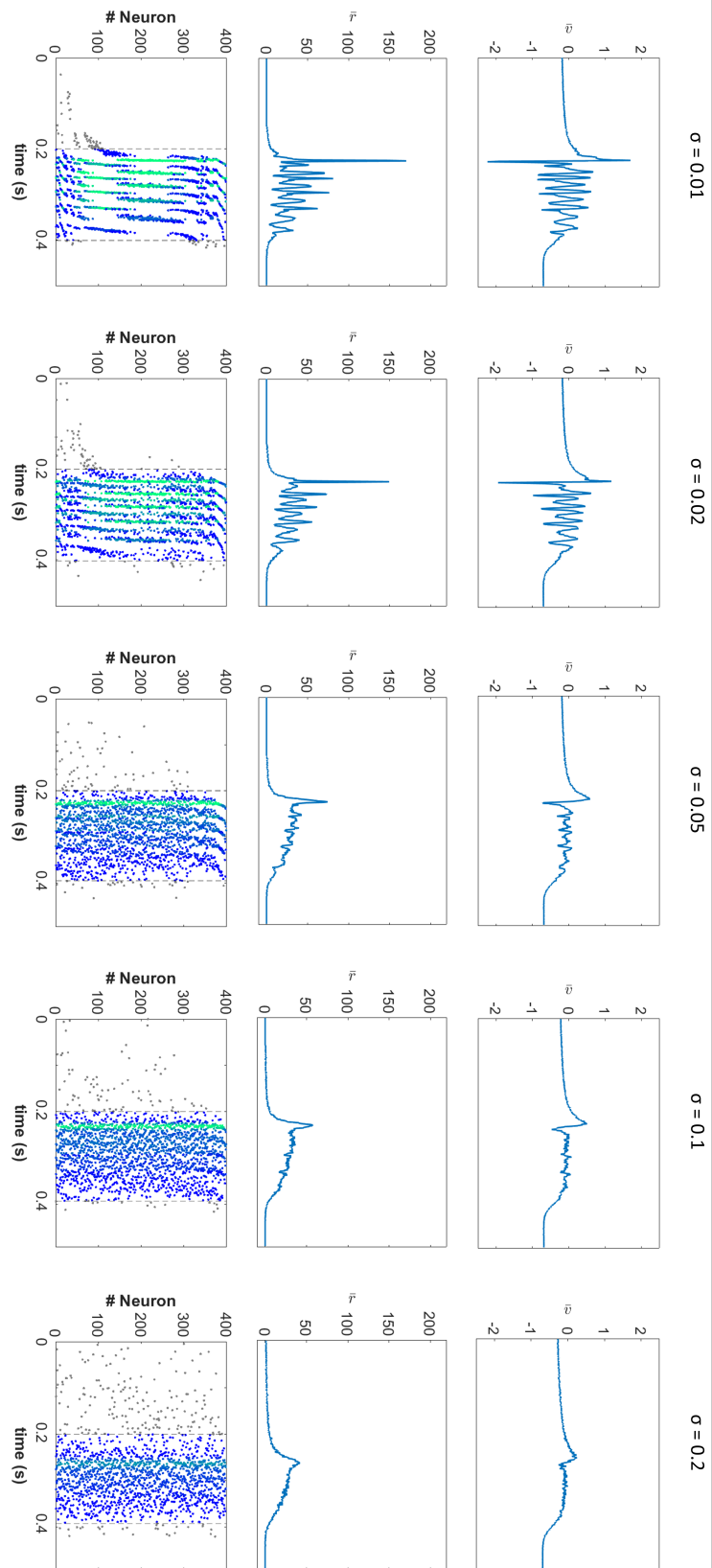
Figure 2: The effect of different values of the standard deviation of individual additive noise σ on burst shape. At the top, middle and bottom, five plots of $\bar{v}$-evolution, $\bar{r}$-evolution and neuron spikes, respectively. From left to right, σ increases. A larger value of σ causes more flattening of the burst shape, and reduces synchrony.
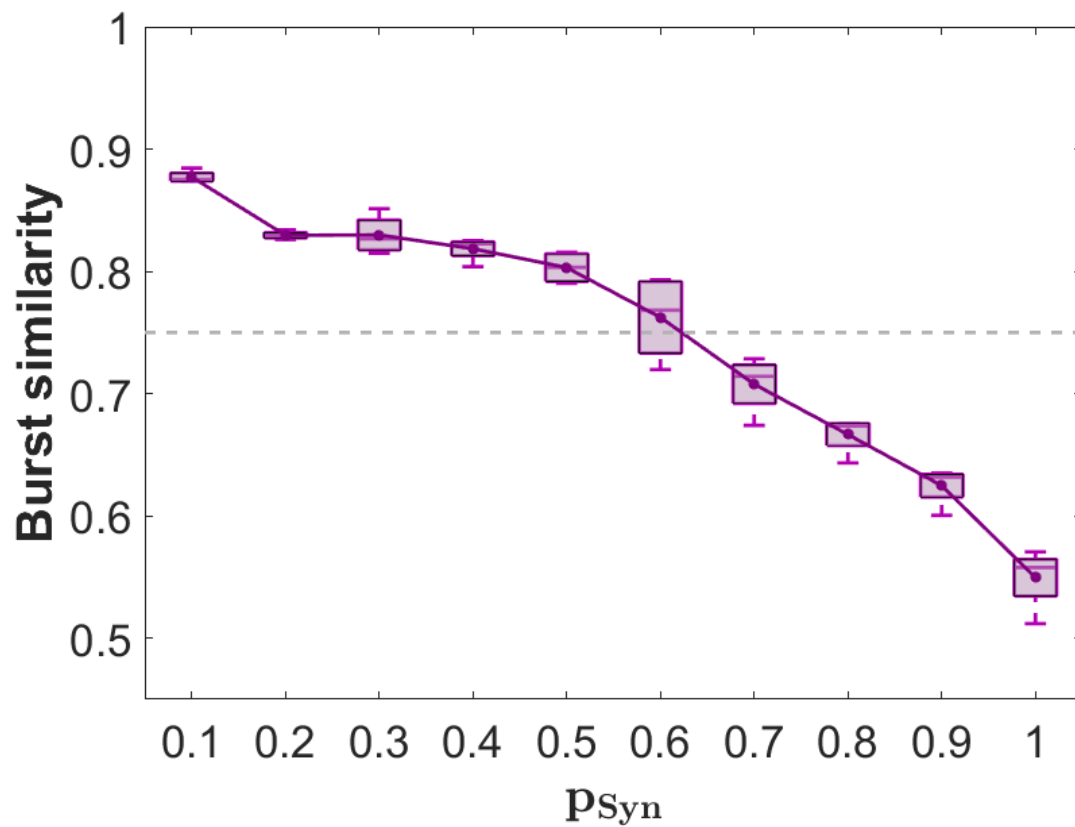
Figure 3: Mean values of burst similarity for simulations of the two-population model with excitation and inhibition, for four different network realisations and for different synaptic coupling probabilities p_{Syn}. The threshold for identical bursts is considered $q = 0.75$, shown as a dashed grey line. Connected purple points show the mean values of q of the different networks for a given p_{Syn}, the purple boxes show the median and quartiles. For $p_{Syn} > 0.6$, the mean values of q are below the threshold for identical bursts.